annalen der physik
www.ann-phys.org

Metasurfaces-Enabled Advanced Multidimensional Imaging: Principle and Applications

Qi Liu, Yongliang Liu, Wenwei Liu, Hua Cheng,* and Shuqi Chen**

The efficient acquisition of multidimensional information—spatial, polarization, frequency, and phase of optical fields, is a key research focus. Metasurfaces, which are emerging as planar arrays of artificial nanostructures, offer significant advantages in advanced imaging due to their exceptional ability to manipulate electromagnetic waves through subwavelength optical resonators. Meanwhile, the rapidly developing computational imaging algorithms have also greatly enhanced the performance of metasurfaces in multi-dimensional imaging. In this review, we focus on the research progress in metasurface-empowered multidimensional imaging, including advanced spatial imaging, compact polarization imaging, high-resolution spectral imaging, single-shot phase imaging, and edge imaging. Their basic principles and imaging results will also be presented. Furthermore, a summary of several current challenges and anticipation in various future directions within this field will also be provided.

1. Introduction

In the field of optical imaging, the pursuit of improving the imaging quality, including resolution,[1] flexibility,[2] and efficiency, is always the key topic for researchers, and lots of remarkable progress has been achieved. In the past decade, with the development of automation, artificial intelligence, and mobile terminals, the requirement for high-performance optical imaging has risen to a new level. To date, it is no longer limited to spatially 2D imaging of the targets but encompasses multiple dimensions such as space,[3–5] spectrum,[6,7] polarization,[8,9] and complex amplitude[10,11] in order to obtain more comprehensive optical information. Some multi-dimensional imaging such as high-spectral imaging,[12–14] depth imaging[4,15,16] has been achieved by using gratings, lens systems, and prisms. However, traditional optical imaging devices still suffer from bulky designs and low efficiency, constraining their ability to simultaneously capture multi-dimensional information about the targets. The emergence of metasurfaces has provided new tools for addressing these challenges.

Metasurfaces, consisting of 2D arrays of subwavelength nanostructures, have revolutionized modern optics by facilitating precise manipulation of light.[17–19] With subwavelength artificial structures known as independently designable meta-atoms, metasurfaces offer remarkable degrees of design freedom, providing unparalleled control over light at the subwavelength scale.[20–23] To better investigate metasurfaces, some theories have been proposed to analyze or explain interactions between light and meta-atoms. For instance, Yu et al. proposed the generalized Snell's law to describe the phase abrupt gradient and beam deflection introduced by metasurfaces[17]; Terekhov et al. performed a multipole analysis of the transmission and reflection spectra of metasurfaces, presenting a half-analytical method for analyzing the scattering properties of the dielectric metasurfaces[24]; Liu et al. conducted an analysis of the field patterns in both real and momentum space,[25] offering insight for functional metasurfaces. These theories provide significant guides to design efficient, multifunctional, and versatile metasurfaces across wide electromagnetic spectra from radio waves to the ultraviolet.

Recently, metasurfaces have demonstrated significant advantages in the multidimensional control of light. As shown in **Figure 1**, due to their local and nonlocal resonances with incident light, metasurfaces can manipulate multiple parameters of light, including phase,[26–28] amplitude,[29,30] frequency,[31–33] polarization,[34,35], etc. at subwavelength scale through the precise design of meta-atoms. Moreover, with advancements in design algorithms and fabrication techniques, metasurfaces enable more complex functionalities and modulation across multiple channels,[36–38] such as multi-channel OAM holography,[39] overcoming the limits of polarization-multiplexing channels,[40] high-quality structural color displays with hybrid dielectric nano-pillars,[41] and multifocal or multi-wavelength metalens imaging.[42,43] Meanwhile, advancements in computational

Q. Liu, Y. Liu, W. Liu, H. Cheng, S. Chen
The Key Laboratory of Weak Light Nonlinear Photonics
Ministry of Education
School of Physics and TEDA Institute of Applied Physics
Nankai University
Tianjin 300071, China
E-mail: wliu@nankai.edu.cn; hcheng@nankai.edu.cn; schen@nankai.edu.cn

S. Chen
School of Materials Science and Engineering
Smart Sensing Interdisciplinary Science Center
Nankai University
Tianjin 300350, China

S. Chen
The Collaborative Innovation Center of Extreme Optics
Shanxi University
Taiyuan, Shanxi 030006, China

The ORCID identification number(s) for the author(s) of this article can be found under https://doi.org/10.1002/andp.202400230

DOI: 10.1002/andp.202400230

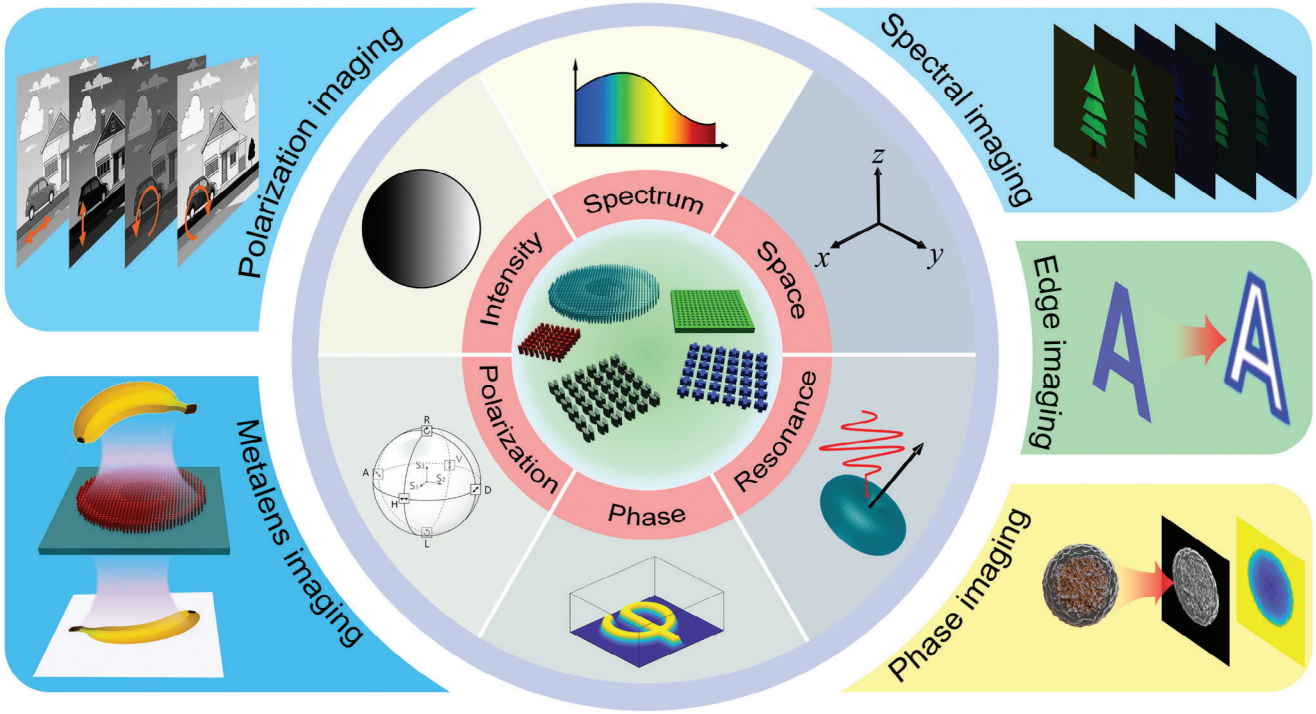

Figure 1. Schematic of the metasurfaces for multi-dimensional imaging. The multi-dimensional information, such as spectrum, intensity, and polarization, can be manipulated by metasurfaces. Based on this multidimensional information, metasurfaces demonstrate significant advantages in polarization imaging, metalens imaging, spectral imaging, edge imaging, and phase imaging.

imaging also offer new methodologies for metasurfaces-based multidimensional imaging. By integrating computational imaging algorithms with the advantages of metasurfaces, researchers can optimize image reconstruction and processing techniques, enabling more accurate interpretation of complex optical information. Techniques such as compressed sensing, machine learning, and image processing algorithms can be employed for tasks such as depth estimation, spectral recovery, phase retrieval, and polarization analysis, significantly enhancing the quality and effectiveness of multidimensional imaging.

Here, we present a comprehensive overview and synthesis of the advancements in metasurfaces for multidimensional imaging. In Section 2, we provide an extensive summary of the fundamental principles governing metasurfaces and their applications in multidimensional imaging, encompassing meta-atom modulation, polarization control, and spectral imaging methods, as well as the basic principles and algorithms of computational imaging. These theoretical foundations establish a framework for the practical implementation of multidimensional imaging. In Section 3, we present the research advancements in optical imaging and depth estimation utilizing metalenses, encompassing developments in single-wavelength metalenses, achromatic metalenses, and metalens arrays for depth sensing and high-precision localization. In Section 4, we introduce the progress of metasurfaces in polarization imaging. We discuss different implementation methods, including using metasurfaces to split polarization states for detection, using polarization filters to achieve polarization imaging, and combining metasurfaces with algorithms to achieve efficient polarization imaging. In Section 5, we introduce the relevant progress of metasurface-based spectral imaging. Based on the detection principles, we discuss several technological approaches, including dispersive metasurfaces, narrowband filtering metasurfaces, and compressed sensing combined with metasurfaces. In Section 6, we give an introduction to the relevant works on metasurface phase imaging. These works are based on principles such as near-field effects, interference modulation, and algorithmic solutions, enabling compact, single-shot phase imaging using metasurfaces. In Section 7, we introduce the basic design ideas of analog optical computing based on metasurfaces, elaborating on the design principles, functional characteristics, and research progress of different analog optical computing. In the end, we summarize the review and discuss the future development of metasurfaces-based multidimensional imaging.

2. Modulation and Imaging Principles of Metasurfaces

Multidimensional imaging presents substantial challenges for the design of optical devices, necessitating innovative approaches to manipulate light across various dimensions. The exceptional design flexibility of meta-atoms allows for a rich array of light-matter interactions, essential for achieving precise control over multiple aspects of light, including amplitude, phase, polarization, and frequency. By harnessing these capabilities, metasurfaces emerge as powerful tools for advancing multidimensional imaging, enabling the simultaneous acquisition and manipulation of diverse optical information.

2.1. Basic Resonances of Nanostructures

To achieve a comprehensive control and analysis of the multidimensional information carried by light, it is imperative to investigate the interaction between incident light and metasurfaces determined by the material properties and the geometric characteristics of meta-atoms. By designing metasurfaces with different materials and meta-atoms, various resonance types can be achieved, such as Mie resonances[44,45] and plasmonic resonances.[46–48] These resonances play a crucial role in determining the optical response of metasurfaces and enable functionalities such as polarization control, spectral filtering, and phase modulation. Understanding these interactions is the foundation for specific imaging and sensing applications based on metasurfaces.

Plasmonic resonances originate from the metasurfaces consisting of metallic-type meta-atoms. When interacting with incident light, such meta-atoms experience a statistical displacement of conduction electrons from their equilibrium positions. This collective motion can be characterized as a Lorentzian oscillator.[49,50] Its distinctive feature includes a peak in displacement amplitude (polarizability) centered around the resonance frequency.[51,52] With such collective motion of electric charges, electric dipoles (ED), magnetic dipoles (MD), and other resonances have been developed to manipulate the incident light. However, the efficiency of plasmonic metasurfaces is limited by ohmic losses. Moreover, their operational wavelength is typically confined to resonances, resulting in limited bandwidths.[21] This narrowband response limits their further applications in broadband imaging, which is required for most imaging scenarios.

The Mie resonance is another type of resonance that occurs when light interacts with a dielectric structure at the scale of λ/n_{eff}, where λ represents the resonance wavelength and n_{eff} denotes the effective refractive index of the dielectric resonator.[53] Interestingly, the effective refractive index and resonance wavelength depend on not only the constitution materials but also the geometry of the resonator. Compared with a plasmonic nanostructure that usually generates a single or very few optical resonances, Mie resonances encompass ED, MD, and higher orders of multipoles, enabling multidimensional manipulation of electromagnetic waves in both near and far fields.[54–56] Moreover, Mie resonances can achieve efficient light manipulation due to the minimal intrinsic losses of the dielectric materials in the working wavelength region.[55]

Expanding the working bandwidth often requires additional complex designs for both plasmonic and Mie resonance metasurfaces.[57,58] Consequently, it is imperative to develop innovative design strategies that can effectively address these limitations and facilitate the operation of metasurfaces across wider frequency ranges, thereby enhancing their suitability for diverse imaging applications.

2.2. Multi-Dimensional Modulation and Detection of Metasurfaces

2.2.1. Phase Modulation of Metasurfaces

The optical phase manipulation with metasurfaces can be classified into 3 kinds, i.e., resonant phase,[59,60] geometric phase,[61,62] and propagation phase.[63,64] Resonant phase arises from resonances such as Mie resonance, Fabry-Pérot resonance, and surface plasmon resonance between incident light and meta-atoms.[65–67] Both dielectric and metallic meta-atoms can be utilized to engineer the optical phase.[68] For instance, the Mie resonance can be induced at a specific wavelength by adjusting the geometric parameters of the dielectric meta-atoms, resulting in a phase shift ranging from 0 to 2π. Due to the low loss and high refractive index of dielectric materials, high-efficiency metasurfaces can be achieved in either transmission or reflection mode, which plays a crucial role in the design of high-performance metasurfaces. The bandwidth of the resonance, however, tends to be narrow compared with traditional phase modulation devices, thereby restricting the working wavelength within a limited range.[44]

The propagation phase associated with the propagation of light inside the resonator provides another phase for designing metasurfaces. When the height of the meta-atom is comparable to the wavelength and waveguide modes exist, the meta-atom can be regarded as a waveguide.[68] Thus, the phase delay of the meta-atoms can be described as $\Phi = 2\pi/\lambda n_{neff} H$, where λ is the wavelength in vacuum, n_{eff} and H are the effective refractive index and height of the meta-atoms. By tuning the geometry cross-section of meta-atoms, the phase can be changed accordingly.

The geometric phase, known as the Pancharatnam-Berry (PB) phase in optics, is independent of the resonances of meta-atoms but related to the orientation angle and symmetry of the meta-atoms.[61,69,70] For incident light with an electric field $\mathbf{E}_{in} = [1 \ \pm i]^T$, the output electric fields E_{out} from the metasurface that can change the polarization state is

$$\mathbf{E}_{out} = A_1 e^{i\varphi_1} \begin{pmatrix} 1 \\ \pm i \end{pmatrix} + A_2 e^{i\varphi_2} e^{\mp i2\theta} \begin{pmatrix} 1 \\ \pm i \end{pmatrix} \tag{1}$$

where $A_1 e^{i\varphi_1}$ and $A_2 e^{i\varphi_2}$ are the coefficient of transmittance which includes the propagation phase,[71] θ is the orientation angle of each meta-atom. The first term on the right-hand side of Equation 1 represents the co-polarized component, while the second term corresponds to the cross-polarized component of the output light with a phase shift of $-2\sigma\theta$ (σ indicates the helicity of the polarization). Therefore, a metasurface with a phase distribution covering 0 to 2π can be achieved by just varying the orientation angle θ as half of the target phase. The powerful phase modulation capability provides a foundation for metasurfaces in fields such as information encryption,[72] high-quality display,[73] and imaging.[74]

2.2.2. Principle of Metasurfaces Polarization Modulation and Detection

Stokes parameters are widely used to describe the polarization state of light, which can be expressed as[75]:

$$\mathbf{S} = \begin{bmatrix} S_0 \\ S_1 \\ S_2 \\ S_3 \end{bmatrix} = \begin{bmatrix} E_x^2 + E_y^2 \\ E_x^2 - E_y^2 \\ 2E_x E_y \cos\delta \\ 2E_x E_y \sin\delta \end{bmatrix} = \begin{bmatrix} I_x + I_y \\ I_x - I_y \\ I_{45^\circ} - I_{-45^\circ} \\ I_R - I_L \end{bmatrix} \tag{2}$$

where E_x, E_y are the electric field vectors in x and y directions, δ is the phase difference of light in x and y directions. $I_{x/y/\pm45°/R/L}$ is the intensity of the x, y, $\pm45°$ linear polarization and right-hand circular polarization (RCP) and left-hand circular polarization (LCP), respectively. S_0 is the total light intensity, S_1 is the difference of the light intensity in x and y polarizations, S_2 is the difference of the light intensity in 45° and −45° linear polarizations and S_3 is the difference of the light intensity in RCP and LCP. Conventionally, only the S_0 component of light can be recorded in an intensity-sensitive imaging process. To obtain additional information about the polarization state, metasurfaces provide a solution through their polarization modulation capacities. In general, polarization detection can be commonly achieved by employing techniques such as splitting or filtering the incident light based on its polarization, as reported by previous research.[35,76,77]

Regarding the method of splitting light, diverse phase profiles of metasurfaces can be computed for the deflection directions of distinct polarization states, since metasurfaces can simultaneously manipulate 2 arbitrary orthogonal polarization states of light by designing anisotropic meta-atoms.[78] Such behavior can be mathematically described with the Jones matrix:

$$\mathbf{J}(x,y) = \begin{bmatrix} e^{i\phi^+(x,y)}\left(\mathbf{p}_1^+\right)^* & e^{i\phi^-(x,y)}\left(\mathbf{p}_1^-\right)^* \\ e^{i\phi^+(x,y)}\left(\mathbf{p}_2^+\right)^* & e^{i\phi^-(x,y)}\left(\mathbf{p}_2^-\right)^* \end{bmatrix} \begin{bmatrix} \mathbf{p}_1^+ & \mathbf{p}_1^- \\ \mathbf{p}_2^+ & \mathbf{p}_2^- \end{bmatrix}^{-1} \tag{3}$$

where $p^{\pm}_{1,2}$ are the electric components of an arbitrary incident orthogonal polarization, and $(p^{\pm}_{1,2})^*$ represents the output polarization is mathematically equal to the complex conjugate of the incident polarization state, $\varphi^{\pm}$ is the phase profile of the corresponding polarization state. Furthermore, the Jones matrix of a birefringent metasurface is[75]:

$$\mathbf{J}(x,y) = \mathbf{R}(\theta(x,y)) \begin{bmatrix} t_x(x,y) & 0 \\ 0 & t_y(x,y) \end{bmatrix} \mathbf{R}(-\theta(x,y)) \tag{4}$$

Where $R(\theta)$ is the rotation matrix with an orientation angle θ of the meta-atoms. Consequently, a high degree of freedom in controlling polarization has been achieved through the precise rotation of anisotropic meta-atoms at a predetermined angle.

Filtering the polarization is also an effective method to obtain the polarization state. For linearly polarized light, anisotropic meta-atoms with different transmission/reflection in 2 polarization directions can be applied to perform as a polarization filter.[79] The realization of circular polarization selectivity typically necessitates the presence of meta-atoms with chiral geometries, facilitating the excitation of distinct resonances under left-handed and right-handed polarization, thereby achieving selective responses to circular polarization. Both 2D and 3D chiral structures can be employed to attain circular polarization selection. This can be achieved through resonance manipulation, utilizing Mie resonance,[80] surface plasmons,[81,82] and non-local effects[83] to achieve an efficient selection of the target polarization with a high extinction ratio.

2.2.3. Principle of Multi-Dimensional Spectrum Detection

Frequency is another important dimension, as it carries intrinsic information about the material. The electric field of the target to be detected at the objective plane can be written as $E(x, y, \lambda)$. The frequency information in the signal is simultaneously captured by each photodiode or sensor in the traditional imaging process, resulting in the loss of most of the frequency information. Designing spectral modulation devices that allow the frequency information to be resolved from the aliasing becomes particularly important.

Conventionally, optical spectra can be acquired by utilizing dispersive elements, such as gratings wherein light undergoes diffraction in various directions for different wavelengths.[84] Subsequently, spectral information can be obtained by employing a sensor to capture the spatially distributed intensity.[85] As the distance of propagation increases, the separation between different frequencies of light also grows, leading to increased spectral resolution. Narrowband filters can also realize spectral detection.[7,86] For example, when using a 2D-arrayed spectral filter, a broadband spectrum can be obtained through an arrayed intensity distribution. By leveraging bound state in the continuums (BICs) based metasurfaces, the linewidth of the resonance as narrow as ≈1 nm can be achieved, and the resonance wavelength can be adjusted by structural parameters.[87–89] Compared with dispersive elements, which require spatial separation of different frequencies, narrowband filters do not necessitate such spatial separation, thereby facilitating the design of more compact spectral sensing systems.

Reconstructive spectral imaging is an emerging technology over the past decade.[90–92] In contrast to dispersion and narrowband filtering, a device designed for spectrum reconstruction can generate a series of wavelength-dependent signature patterns. The intensity array containing spectral information can be captured by sensors through a spectral-to-spatial mapping, which is expressed as[7]:

$$I(\mathbf{x}) = \int_{\lambda_1}^{\lambda_2} p(\lambda, \mathbf{x}) \cdot s(\lambda)\, d\lambda \tag{5}$$

where $s(\lambda)$ is the input spectrum, $p(\lambda, x)$ is the spectrum patterns of the device and the process of detection involves the integration over the wavelength λ ranging from λ_1 to λ_2. When the position and wavelength are discretized into a matrix, Equation (5) can be written as:

$$\mathbf{I} = \mathbf{P} \cdot \mathbf{S} \tag{6}$$

where the spectrum S can be reconstructed by solving underdetermined linear equations. Typically, obtaining higher spectral resolution information requires increasing the number of wavelengths in the equations. Techniques such as compressed sensing, deep learning, and convex optimization can be employed to reconstruct the spectrum with a high accuracy. Detailed examples are discussed in Section 5.

By delicately designing the metasurface with the utilization of these principles, high-quality detection of the optical field in multiple dimensions can be achieved.

2.3. Computational Imaging for Metasurfaces

The traditional point-to-point relationship between an object and its conjugate image is inadequate for addressing the complexities

of comprehensive multidimensional imaging, primarily due to the aliasing of multidimensional information at the image plane.[93] To effectively separate this aliasing information, various computational imaging methods have been developed over the past decades. By introducing encoding in the object plane, within the diffractive process, or at the detector plane of the imaging system, it becomes possible to reconstruct the object's information by solving the inverse problem associated with the encoded imaging process.[94]

The forward imaging process can be succinctly represented as $y = H(x) + \epsilon$, where y is the observed data, H denotes the operator of the imaging system, ϵ is the noise of the imaging system, and x represents the object. The aim of computational imaging is to solve $y \rightarrow x$, which can be considered an inverse problem.[95] Due to the inevitable loss of information during the detection process, the inverse problem is often ill-posed. This results in the non-uniqueness of the solution, indicating that it is hard to uniquely determine a single x solely based on y. To solve this inverse problem, some algorithms have been developed and performed well in computational imaging tasks.

When the physical imaging process H is known, the solution to the inverse problem can be obtained by iteratively solving the following Lagrange-type equation:

$$x = \operatorname{argmin} \left\| y - H(x) \right\|_2^2 + a\Phi(x) \tag{7}$$

Where the first term represents the constraint between the detected signal and the physical process. a is constant and $\Phi(x)$ is the regularization term that introduces prior constraints, such as norm or smoothness constraints, to prevent overfitting of the solution. In solving imaging problems, several algorithms based on this framework, such as least squares methods[96] and compressed sensing,[97–99] have demonstrated exceptional performance in fields like spectral imaging[97] and super-resolution imaging.[100] However, several disadvantages still persist, including the time-consuming nature of iterative solving, convergence issues, and the impact of noise on the solutions. These factors limit the applicability of these methods in real-time imaging scenarios.

Another approach is to solve the problem using data-driven methods. For an imaging system, a data set corresponding to the detected signal can be first established from the true value of object information.[94,101] Using a deep neural network, the inherent physical process of the imaging system can be "learned" from the obtained large amount of prior data and the mapping R can be established as follows:

$$R : y \rightarrow x \tag{8}$$

this method can achieve image reconstruction through the training of a neural network when the imaging physical process is unknown. And it can solve some problems in extreme environments.[102,103] Moreover, this method is non-iterative and can achieve real-time imaging. However, this method also faces disadvantages such as poor generalization and poor interpretability, which limit its applications.

To overcome the shortcomings of the above 2 methods, significant advancements have been made in recent years by integrating both approaches. Significant advancements have been made in recent years by integrating both approaches. For instance, fine-tuning a pre-trained neural network with a physical model can mitigate overfitting and reduce the probability of prediction errors.[104] This synergistic approach, which combines model-driven and data-driven methodologies, aims to transcend the constraints of traditional techniques, thereby enhancing the practical applicability of computational optical imaging technologies.

The previously mentioned methods predominantly focus on processing digital signals acquired from imaging systems. However, recent developments have shown substantial progress in directly manipulating the incident light field through optical techniques. For example, optical neural networks exploit the correspondence between input and output light fields, employing inverse design algorithms to optimize material distribution at each layer.[105,106] This enables operations such as classification, encryption, and feature extraction of the input light field. The processing speed of these optical systems significantly surpasses that of digital signal processing performing analogous functions, as the input light field propagates at the speed of light.

Computational imaging integrates "computation" into the optical imaging process or its results, employing algorithms to reconstruct information about the object. With the flexible manipulation capabilities of metasurfaces over incident light across multiple dimensions and channels, computational imaging has emerged as a vital tool in the realm of multidimensional imaging enabled by metasurfaces.

3. Spatial intensity Imaging

One of the primary goals of imaging is to capture the spatial intensity information distribution of an object, with lenses playing a crucial role in this process. By leveraging the conjugate relationship between the object and image planes, it is possible to obtain the two-dimensional intensity distribution of the object. Furthermore, employing methods such as lens arrays allows for the acquisition of three-dimensional intensity information distributions, enhancing our understanding of the object's structure and spatial characteristics. However, traditional lenses are facing challenges such as bulk size and aberrations. With the development of nanotechnology, the theory and design methods for metasurfaces used to achieve lens functionality, known as metalenses, have gradually been refined.[107–109]

Metalens is a kind of metasurface with precisely arranges each meta-atom according to the spatial phase distribution[110]

$$\Phi(r, \omega) = -\frac{\omega}{c}\left(\sqrt{r^2 + f^2} - f\right) \tag{9}$$

where r represents the distance between each nanostructure and coordinate origin located at the center of the metalens, f is the focal length, ω is the angular frequency of the incident, and c is the light velocity in vacuum. The basic task of designing metalens is to arrange the phase of the meta-atom so that their phase satisfies Equation 7. The numerical aperture (NA), which denotes the light-focusing capability of a lens, is mathematically defined by $\mathrm{NA} = n\sin\alpha$, where n represents the refractive index of the surrounding medium of the metalens, and α signifies the half-angle encompassing the maximum divergence

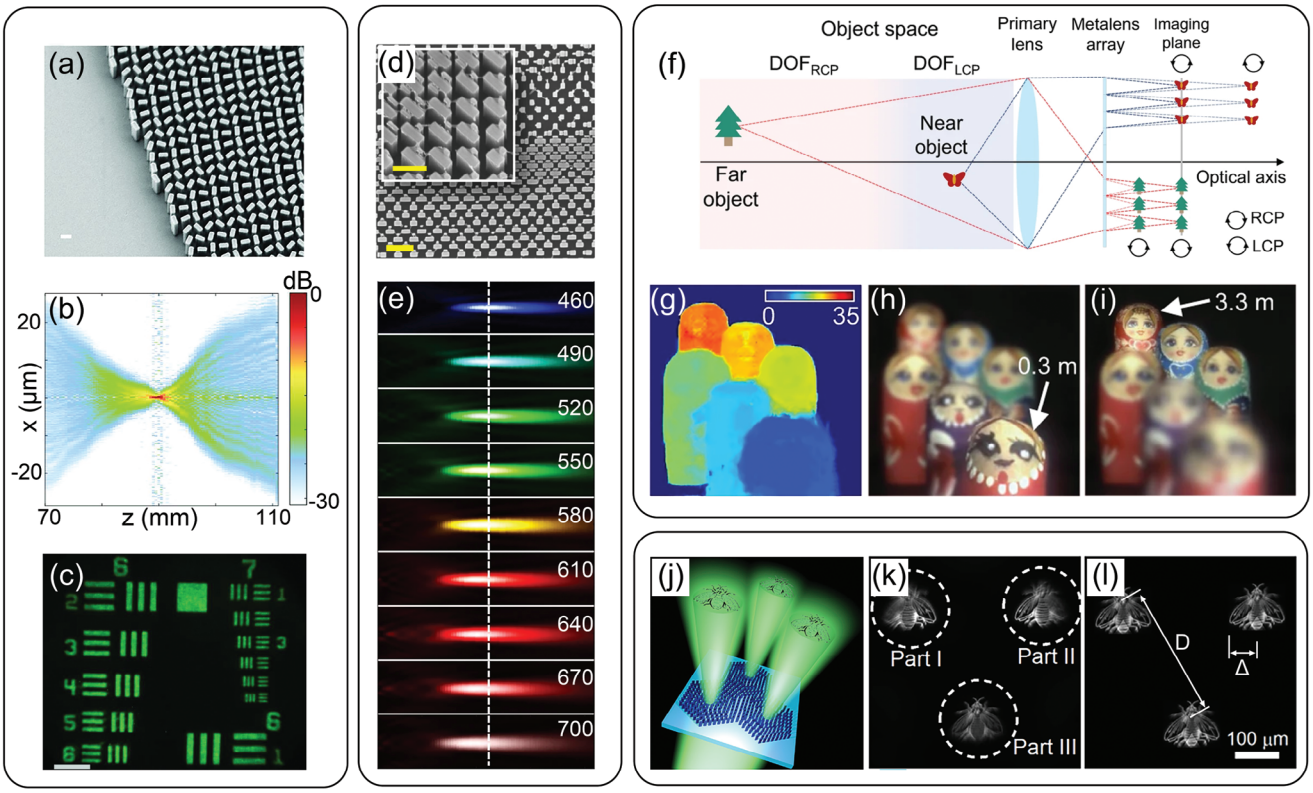

Figure 2. Metalens imaging. a) SEM image of metasurface lens composed of rectangular TiO_2 nano-pillars; b) The x-z plane intensity distribution of the focused beam evolution in a 40 mm range, 20 mm before and after the focal point; c) Imaging of the resolution chart with metalens; d) SEM image and its local magnification of achromatic metalens; e) Achromatic focusing at different wavelengths in the visible region; f) Schematic of the bioinspired photonic metalens array, by leveraging the dispersion of the metalens and different focal lengths for RCP and LCP. A large depth of field ranging from 3 cm to infinity can be achieved; g–i) Disparity estimation results and refocused images at different depths with the bio-inspired photonic metalens array; j–l) Single-shot aberration-corrected 3D positioning metalens array. (a-c) Reproduced with permission.[111] Copyright 2016, American Association for the Advancement of Science. (d, e) Reproduced with permission.[120] Copyright 2019, Springer Nature. (f-i) Reproduced with permission.[127] Copyright 2022, Springer Nature. (j-l) Reproduced with permission.[128] Copyright 2020, Optical Society of America.

angle of the light processed by the lens. The resolution of a lens can be defined as the minimum size of features that can be resolved in an image, which can be written as $d \approx 1.22\ \lambda\ \mathrm{NA}^{-1}$. Thus, the imaging resolution increases for larger NAs. In 2016, Khorasaninejadproposed a dielectric metalens with diffraction-limited focusing,[111] as shown in **Figure** 2a. Millions of sub-wavelength TiO_2 nanopillars were fabricated on the substrate, and each nanopillar's rotation follows the geometric phase rule where the rotation angle is half of the design phase. With cross-polarized components of RCP and LCP incident light focused, as shown in Figure 2b, the metalens with a diameter of 240 μm and an NA of 0.8 was fabricated to image with sub-wavelength resolution in the visible region. The imaged USAF 1951 resolution chart by the metalens is shown in Figure 2c. In the last few years, there have been many advances in metalens, such as near-unitary-NA metalens,[112] centimeter-scale metalens,[113,114] ultraviolet metalens,[32,115] device-integrated metalens.[116]

Achieving achromaticity is one of the objectives in the design of broadband lenses. Because of the dispersion of the meta-atoms, the presence of chromatic aberration limits the further application of metalens. In 2015, Aieta et al. analyzed the phase characteristics of subwavelength resonant units, performed phase compensation for each design wavelength, and achieved achromatic focusing at 3 wavelengths by adjusting the parameters of the meta-atoms.[117] This method has been refined by dispersion engineering, which is applied to metasurface design to achieve achromatic metalenses.[118] The dispersion relation can be analyzed through a Taylor expansion of Equation 7 around angular frequency ω_0:

$$\Phi(r,\omega) = \Phi(r,\omega_0) + \left.\frac{\partial\Phi(r,\omega)}{\partial\omega}\right|_{\omega_0}(\omega-\omega_0) + \left.\frac{\partial^2\Phi(r,\omega)}{2\partial\omega^2}\right|_{\omega_0} \times (\omega-\omega_0)^2 + \cdots \tag{10}$$

where the first and second-order derivative terms are the group delay and the group delay dispersion. By matching $\Phi(r,\omega_0)$, $\partial\Phi(r,\omega)/\partial\omega$, and $\partial^2\Phi(r,\omega)/2\partial\omega^2$ with meta-atoms, metasurfaces can be designed to significantly compensate for the dispersion.[119] For example, the phase and the group delay can be changed by adjusting the geometric parameters of dielectric meta-atoms (Figure 2d).[120] Combined with polarization multiplexing, metalenses can achieve polarization-insensitive chromatic aberration correction for focusing, as shown in Figure 2e. Achromatic imaging of a resolution chart has also been demonstrated using the achromatic metalens, which significantly

promotes their applications such as bioimaging,[121] fiber integration[122], and virtual reality[123] for high-quality imaging. Furthermore, some strategies on achromatic metalens design have been proposed to enable achromatic metalens with large areas, high NA, and broad bandwidth. For instance, Xiao et al. achieved achromatic metalens covering 400 to 1100 nm at the centimeter scale through frequency-domain coherence optimization.[124] Chen et al. realized the achromatic range of 400–1500 nm with an NA of 0.55 by extending the group delay theory.[125] Li et al. employed the inverse design to realize large-area achromatic metasurfaces for virtual reality applications in visible light. [123]

The potential of metalenses extends beyond these achievements. In the acquisition of three-dimensional intensity information, the integration of rapidly advancing computational imaging algorithms with metalenses has led to significant progress in capturing the spatial characteristics of light fields. This synergy not only enhances the resolution and accuracy of spatial data but also enables the exploration of complex three-dimensional structures with unprecedented detail. In 2019, Lin et al proposed an achromatic light field camera.[126] By arranging a 60 × 60 achromatic metalens array with a diameter of 21.65 um for each, achromatic imaging of the light field camera was achieved for the first time, which is difficult to achieve with traditional microlens arrays. In the light-field camera depicted in Figure 2f, each metalen focuses (RCP) and (LCP) light at different positions through a polarization multiplexing design of meta-atoms.[127] By leveraging the dispersion properties inherent to this metalens array, this setup enables depth-of-field light field imaging from 3 cm to near-infinity. To obtain an in-focus image, a pre-trained deep convolutional multiscale neural network is used for sub-image deblurring. Furthermore, as different metalens at different positions can capture various optical information, disparity estimation algorithms can be utilized to estimate the disparity of objects, which is correlated with the depth of the objects. The estimated disparity result is shown in Figure 2g. With this disparity distribution, the refocus light field images at different depths (Figure 2h,i) are rendered from the original metalens array image. Additionally, by integrating optimization algorithms with the physical processes of imaging, metalens array can be employed to achieve aberration correction and high-precision 3D localization of objects (Figure 2j–l). Liu et al. arranged 3 metalenses as arrays and proposed a gradient descent algorithm based on cross-correlation to eliminate various aberrations including distortion, coma, astigmatism, and field curvature. [128] Simultaneously, they achieved high-precision 3D positioning with an accuracy of ≈1%.

The development of metalens represents a significant advancement in the field of optics. With their unique properties and capabilities, metalens hold great promise for a wide range of applications, from high-resolution imaging to advanced optical systems.

4. Polarization Imaging

Polarization, which describes the direction of electric field oscillation, is an important characteristic in the context of multidimensional imaging. Polarization detection and imaging are of great interest in many areas including materials science, target identification, and bio-sensing. Compared to conventional cameras that only capture light intensity, polarization imaging can reveal additional information, such as stress distribution and surface morphological characteristics. To obtain an image with polarization distribution, there have been several traditional devices-based solutions. For instance, a metallic grating with selective transmission for linear polarization can be fabricated on the pixel of an image sensor to detect a specific polarization.[9] By arranging gratings with different polarization selectivities, an image with polarization information can be obtained. With the arrangement and combination of prisms and polarizers, full Stokes parameters imaging can also be achieved by splitting different polarization into different detectors.[129] However, the performance of traditional polarization imaging approaches is limited by the large size of the components or low energy utilization efficiency. In recent research, metasurfaces offer unique opportunities for polarization manipulation, enabling the realization of compact, lightweight, and high-performance polarization imaging systems.[130–132] In 2012, Yu et al. achieved a broadband (5–12 um) quarter-wave plate by designing the arrangement of V-shaped metal meta-atoms, and the output light had a high degree of circular polarization of > 0.97. This provided an important basis for the polarization detection of metasurfaces.[133]

Polarization imaging metasurfaces require meta-atoms to exhibit different responses for different incident polarizations, which can be achieved by constructing a birefringent meta-atom. In 2015, Anders et al. designed a phase-gradient birefringent metasurface for simultaneous detection of Stokes parameters.[35] The rectangular gold meta-atoms were fabricated on top of a glass spacer and a gold substrate, where the birefringent characteristics can be utilized to separate different polarization states into designed diffraction orders. Meta-atoms with a chiral feature also can realize full-dimensional independent manipulation of circular-polarized waves. Li et al. designed a chiral mirror metasurface using aluminum, achieving spin- and wavelength-encoded imaging of the intended patterns.[134] Furthermore, achieving compact and integrated polarization imaging has also attracted researchers' attention. In 2016, Rubin et al. used the theory of matrix Fourier optics, which incorporates the Jones matrix into the Fourier expansion of the optical field.[135] In addition to providing information about amplitude and phase, matrix Fourier theory also describes the behavior of polarization, which provides guidance for designing polarization diffraction devices. To realize the polarization imaging as depicted in **Figure 3**a using dielectric metasurfaces, they engineered the phase distribution of meta-atoms to satisfy the Jones matrix requirements. These meta-atom arrays were utilized to realize a grating with larger diffraction angles according to the design principles of matrix Fourier theory. As shown in Figure 3b, the metasurfaces can experimentally achieve the polarization imaging, the S_0 component, azimuth of the polarization ellipse (in degrees), and S_3 component of the object are calculated from the image obtained by the metasurfaces. The theory they proposed and metasurfaces greatly facilitate the polarization imaging, so that the full Stokes parameter imaging device can be integrated into a compact device maintaining a high accuracy.

Additionally, other methodologies have also been showcased utilizing metasurfaces for the purpose of polarization imaging. Basiri et al. drew inspiration from the remarkable circular polarization vision of mantis shrimp, characterized by a top reticular cell and 7 bottom reticular cells within their compound eyes.[136]

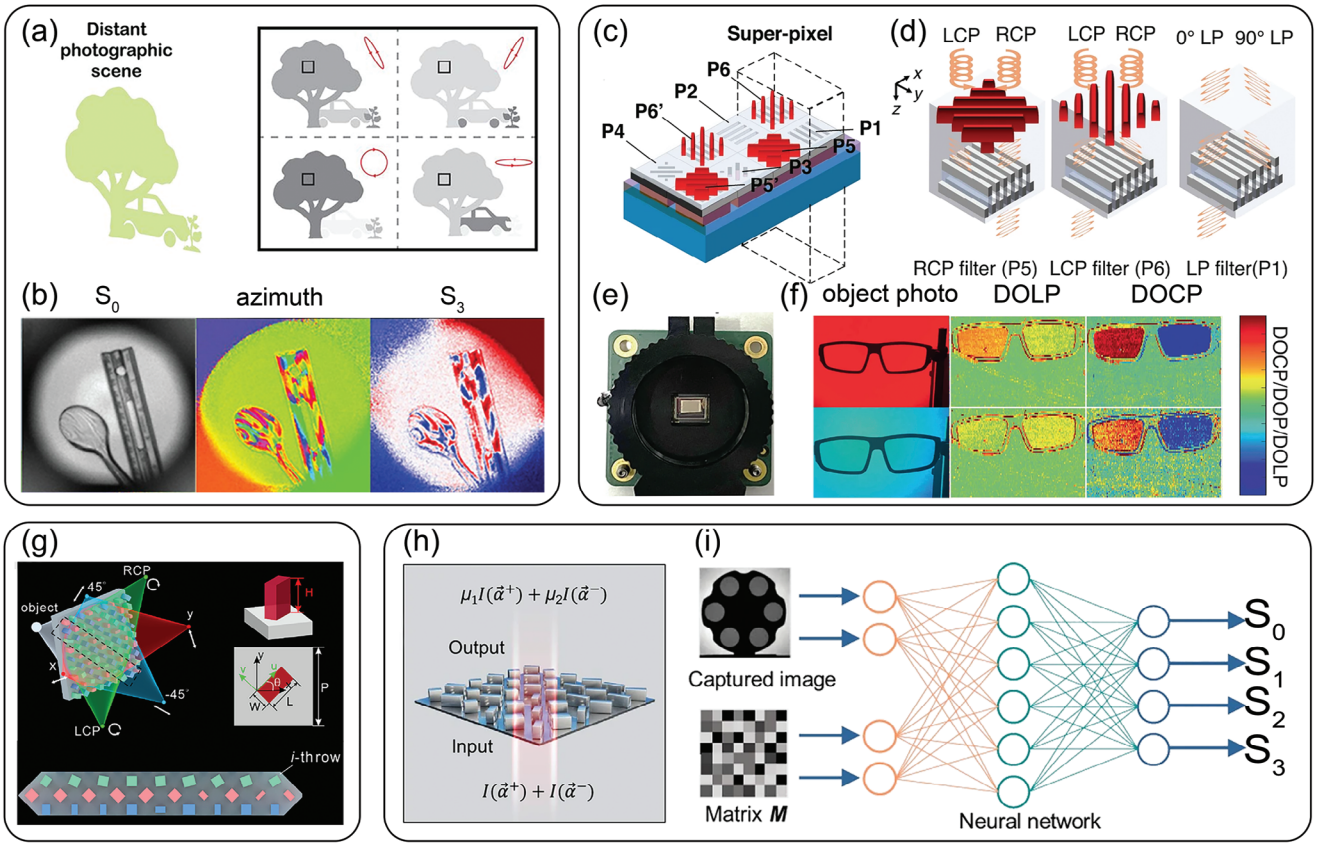

Figure 3. Metasurfaces enabled compact polarization imaging. a) Full Stokes parameters imaging through matrix Fourier transmission theory with dielectric metasurfaces; b) The measured S_0 component, azimuth of the polarization ellipse (in degrees), and S3 component of the object; c) Schematic of the chip integrated full-Stokes imaging metasurfaces, where 6 types of filters were integrated on the CMOS chip to realize the full-Stokes imaging; d) The RCP, LCP and different linearly polarized light realized by different metasurfaces were selectively transmitted to CMOS pixels; e) The CMOS integrated full Stokes polarization camera; f) The images of the degree of linear polarization (DOLP) and the degree of circular polarization (DOCP) of the glasses with the different background colors; g) Dielectric metasurfaces achieving polarization imaging by focusing different polarizations at different position through meta-atoms interleaved arrangements; h) Disordered metasurface-enabled single-shot full-Stokes polarization imaging; i) The reconstruction of polarization states by the convolution neural network. (a, b) Reproduced with permission.[135] Copyright 2019, American Association for the Advancement of Science. (c-f) Reproduced with permission.[137] Copyright 2022, Springer Nature. (g) Reproduced with permission.[138] Copyright 2023, American Chemical Society. (h, i) Reproduced with permission.[139] Copyright 2023, Springer Nature.

They use a single-layer metallic grating to perform as a linear polarization filter, changing the orientation angle to selectively transmit the 0, 45°, 90°, and 135° polarized light. A bilayer structure comprising a metallic grating layer and a dielectric birefringent metasurface layer was designed to mimic the dual-layered configuration found in compound eyes to filter the circular polarization. The dielectric meta-atoms in the first layer are oriented at an angle of 45°to convert circular polarization into linear polarization. Subsequently, the converted linear polarization is filtered by the metallic grating. The distinction between RCP and LCP can be determined by the orientation angle of the meta-atoms, which is either 45°or −45°in the metasurface, respectively. Through the design of bioinspired metasurfaces, the coordinates on the Poincaré sphere of an unknown polarization state can be efficiently and accurately determined. In this way, the bilayer metasurfaces array can also be integrated into an image sensor, where each polarization filter cell corresponds to a sensor pixel.[137] As shown in Figure 3c, Zuo et al designed on-chip full-Stokes imaging metasurfaces. The schematic diagram of the linear and circular polarization filter is illustrated in Figure 3d, featuring a bilayer metasurface consisting of a linear polarization grating and birefringent dielectric metasurfaces, similar to the one mentioned above. The slight difference lies in the proposal of a double-layer metallic polarization grating to replace the single-layer structure grating mentioned above, aiming for a higher linear polarization extinction ratio. The integration is achieved by first fabricating the metasurfaces, and then bonding the metasurfaces on a commercial image sensor (SONY IMX 447) with a 200 nm thick UV resistor, as shown in Figure 3e. In Figure 3f, they also demonstrate polarization imaging of a pair of glasses against different background colors and calculate the degree of linear polarization (DOLP) and the degree of circular polarization (DOCP) of the images. The chip-integrated polarization imaging metasurfaces exhibit remarkable characteristics including compactness, high speed, exceptional detection accuracy, wide field of view, broad bandwidth, and feasibility for large-scale fabrication. These features render them highly promising for a diverse range of applications.

Furthermore, another design by Huang et al. for polarization imaging with metasurfaces is illustrated in Figure 3g, where an interleaved metalens with an NA of 0.51 is employed to spatially focus the x/y, 45°/−45°, and LCP/RCP light at distinct positions.[138] According to the experiment results, the polarization imaging metalens achieved the resolution of 1.2-fold wavelength, which is not achieved in previous metasurfaces-based polarization imaging. Recently, with the advancement of deep learning, deeper information contained within original data has become increasingly feasible. Fan et al. proposed a disorder metasurfaces for single-shot full Stokes parameters imaging.[139] As shown in Figure 3h, by leveraging the weak dichroism induced by varying the in-plane orientation and size of meta-atoms, the output light contains polarization information encoded by the metasurface. Then the Stokes parameters image are reconstructed by employing a compressive sensing algorithm in conjunction with a neural network, as shown in Figure 3i. With the disorder design of metasurfaces, more efficient polarization responses are achieved compared with traditional polarization filter designs.

In summary, metasurfaces-enabled polarization imaging has greatly improved the efficiency of polarization imaging. It offers new approaches to manufacturing more compact and efficient polarization imaging devices and holds great significance in fields such as biological detection and material recognition.

5. Spectral Imaging

Spectra, which convey information about light frequencies, serves as a tool to investigate the absorption, transmission, and reflection properties of materials.[13,140] Spectral imaging, as an emerging multidimensional imaging technology that integrates both spectral and spatial information, plays a pivotal role in diverse domains such as remote sensing,[13] biomedical imaging,[85] material analysis,[141] and astronomical observation.[84] The analysis of spectral signatures across various wavelengths offers valuable insights into the composition, structure, and dynamics of a target. Spectral imaging offers researchers a potent tool to elucidate the interaction between light and matter. Some spectral imaging methods, such as grating dispersion, filter combinations, and Fourier transform spectroscopy, although capable of acquiring both spectral and spatial information, face challenges of bulky size and relatively low spectral and spatial resolutions.[7] Fortunately, metasurfaces have made significant progress in recent years, and have emerged as promising solutions for achieving high-performance spectral imaging. When combined with advanced computational imaging techniques, metasurfaces can further enhance the performance of spectral imaging, enabling the reconstruction of high-resolution images and more detailed spectral information extraction from complex datasets.

One method for measuring spectra and achieving high spectral resolution is to leverage the dispersive properties of devices, which are also utilized in spectrometers. By engineering the dispersion of metasurfaces, compact spectrometers can be developed to greatly reduce the size required for spectral measurements. In 2016, Khorasaninejad et al. designed an off-axis metalens with super-dispersive properties for compact high-resolution spectroscopy.[74] This metalens exhibits a large angle of focusing up to 80°, enabling exceptional spectral resolution in incident wavelength detection within a highly compact configuration. The results of the spectral resolution experiment demonstrate that the metalens is capable of resolving a wavelength separation of 200 pm, which provides an important foundation for spectral detection of metasurfaces. Similarly, dispersion engineering also can be applied in in-plane waveguide optics. Zhang et al. designed a meta-waveguide to reconstruct the spectrum of input light in a 100 × 100 μm region.[142] By utilizing an inverse design algorithm, a highly dispersive and compact five-layer in-plane metalens is constructed in a folded configuration. Spectra in a range of 1525–1575 nm can be reconstructed at a resolution of 0.108 nm. Furthermore, to obtain the 3D spatial information and one spectral information, Hua et al designed a spectral light-field imaging (SLIM) device with a 4 nm spectral resolution and near-diffraction-limit spatial resolution.[143] The SLIM device consists of multiple metalenses with a transversely dispersion as depicted in **Figure 4a**, where the spectral and spatial information can be reconstructed from the dispersive light-field image. Due to the inevitable aliasing of dispersion and spatial information, which leads to image blur, they proposed a convex optimization algorithm to reconstruct the target's spectral information and perform deblurring on the image. The reconstructed refocus image of the letters "META" is shown in Figure 4b–e, where the image at different depths is calculated through light-field refocusing, and the spectrum of marked points in the images is also compared with the commercial spectroscopic camera. Additionally, a spectral super-resolution neural network is also employed to improve the spectral resolution of the SLIM.

Narrow-band filters interact significantly only with specific wavelengths of light, showing narrow bandwidth in the spectrum, which can be applied for spectrum reconstruction. In recent research of resonant metasurfaces, a narrowband spectrum can be obtained by some resonance, such as Fano resonance, Mie resonance, Fabry-Pérot resonance, and quasi-BICs.[65,144] These resonances can achieve comparable filtering effects to conventional filters while maintaining a single-layer structure and offering new possibilities for high-performance spectral imaging. For instance, Tittl et al. proposed an image-based molecular barcoding with dielectric metasurfaces, which can be used in chemical identification.[145] They demonstrated high-Q ($Q > 200$) resonance metasurfaces by utilizing a collective behavior of Mie resonances. As shown in Figure 4h, the unit cell of the metasurfaces consists of 2 elliptic nanopillars with the parameters of A, B, Px, Py, and S, where the resonance peak can be adjusted from 1370 to 1770 cm^{-1} by changing the scaling factor S. The assignment of distinct resonance characteristics to different positions establishes a systematic correlation between spectral and spatial information. By comparing the imaging-based readout of spatially encoded vibrational information before and after target analyte molecules are coated, the molecular footprint can be identified. Moreover, Yesilkoy et al. have successfully integrated dielectric metasurfaces with hyperspectral imaging to establish an exceptionally sensitive label-free analytical platform for biosensing.[146] Since the existence of the quasi-BICs state, a high-Q resonance can be generated under x-polarized incidence by controlling the asymmetry parameters of the unit cell composed of 2 tilt nanopillars. Such metasurfaces were integrated into an image sensor to perform image-based biomolecule

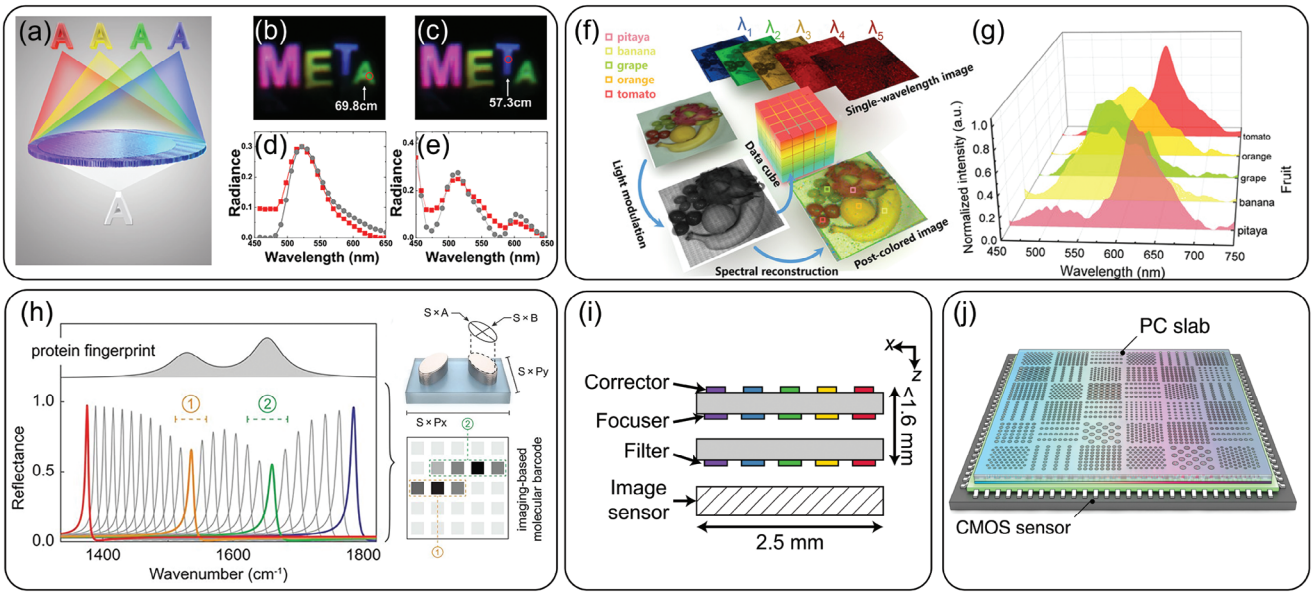

Figure 4. Compact spectral imaging supported by metasurfaces. a) Schematic of the metalens with transverse dispersion; b–e) Refocused images at different depths and the reconstructed spectra of the marked points; f) Snapshot ultraspectral imaging process for a plate of fruit, including the light modulation, spectral reconstruction, assembling as a data cube and output post-colored image; g) Spectra of the marked point in (f); h) The envelope of metapixel reflectance amplitudes replicates the absorption footprint of an input spectrum through the high-Q resonance metasurface; i) The schematic of the parallel spectral imaging metasystems; j) Schematic of the spectrometer composed of the photonic crystal slab and a CMOS sensor. (a-e) Reproduced with permission.[143] Copyright 2023, Springer Nature. (f, g) Reproduced with permission.[149] Copyright 2023, Wiley-VCH. (h) Reproduced with permission.[145] Copyright 2018, American Association for the Advancement of Science. (i) Reproduced with permission.[147] Copyright 2020, American Association for the Advancement of Science. (j) Reproduced with permission.[148] Copyright 2019, Springer Nature.

detection. With the narrow bandwidth (≈2 nm) of the metasurfaces array, they achieved a detection sensitivity with a level of less than 3 molecules per μm^2. Additionally, narrowband filters can also be combined with a metalens array for a compact, aberration-free color camera (Figure 4i). Mcclung et al. designed a parallel metasystem in which 3 layers of metasurfaces act as a corrector, a focuser, and a filter respectively, which can be integrated into an image sensor.[147] Analyzing the sub-images of the metasystems allows for the acquisition of 3D data cube: spatial x, y, and wavelength λ.

Reconstructive spectrum imaging is an emerging direction with the advancement of algorithms and the increase in computational power. In Figure 4j, a photonic crystal slab was integrated into a complementary metal-oxide semiconductor (CMOS) image sensor by Wang et al.[148] Each sub-region of the slab relates to a unique spectrum, which can be pre-measured as a measuring matrix. Solving the measurement process by minimizing regularized squares error with non-negative constraints, the spectrum of incident can be reconstructed with a resolution of ≈1 nm. Furthermore, Yang et al. proposed a metasurface for ultra-spectral imaging, where a series of freeform-shaped metasurfaces are used to improve the spectral diversity.[149] 400 kinds of metasurfaces are designed to be arranged into a unit cell for spectral reconstruction. The reconstruction process is illustrated in Figure 4f,g, where the ultra-spectral imaging metasurface is employed to modulate the light emitted by the target fruits, followed by the application of a reconstruction algorithm to obtain a data cube with dimensions x, y, and wavelength λ. To expedite spectral reconstruction, they also trained a neural network consisting of an encoder and a decoder. During spectral reconstruction, only the trained decoder is utilized.

Metasurfaces have shown great potential in spectral imaging. Various methods like dispersion engineering, narrowband filters, and reconstructive spectrum imaging have been developed, offering high performance and new possibilities in different applications. However, there is still room for improvement in issues such as spectral resolution and dispersion of oblique incidence in metasurface spectral imaging. The application of deep learning in the design and optimization of metasurfaces may contribute to better solving these problems.

6. Phase Imaging

The acquisition of phase information from objects has been a challenge for advancing multidimensional imaging, as most image sensors are only sensitive to the intensity of the light but not the complex amplitude. Over the past century, many approaches have been proposed to obtain the phase information. For instance, Zernike invented phase contrast microscopy which can obtain the contrast image for transparent objects in 1934.[150] The phase information can be converted into intensity information using a phase plate through interference; In 1967, Goodman proposed a method to record the intensity and phase information with digital holography[151]; In 1984, Srinivasan et al. utilized a phase-shift method to achieve measurement of the surface height with a resolution better than 10 μm by reconstructing the phase information[152]; In 2004, Rodenburg proposed an iterative phase retrieval method to obtain the intensity and

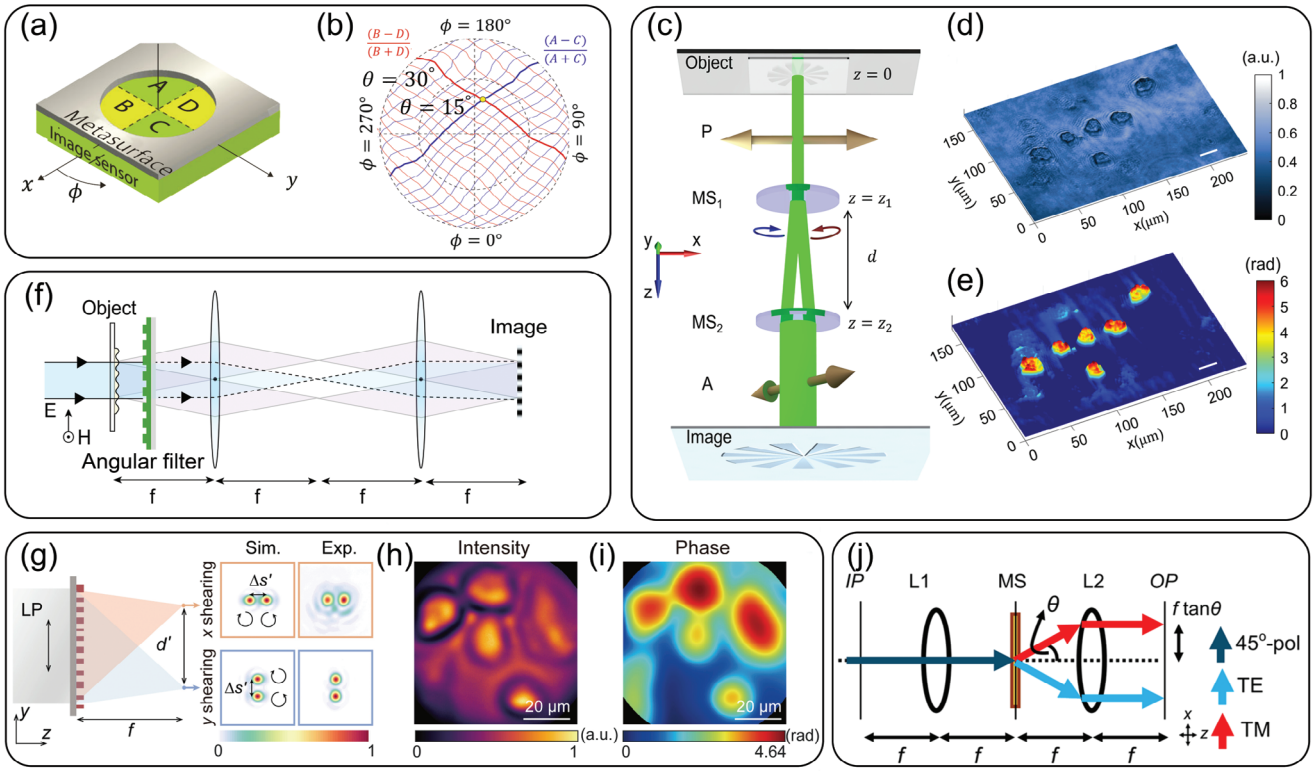

Figure 5. Phase imaging with metasurfaces. a) Schematic of an angle-based CMOS integrated wavefront sensor; b) Contour lines of the intensity ratio from 4 CMOS pixels under the metasurface cell for reconstructing the incident angle; c) Single-shot quantitative phase gradient imaging metasurfaces pair; d, e) Measured amplitude and phase gradient of SKNO-1 cells; f) Non-local based quantitative phase contrast imaging; g) Single-shot complex amplitude imaging by a single-layer metalens, the operation principle of the complex amplitude imaging metalens (left), simulation and experimental profile at the focus plane of the designed metalens (right); h, i) Reconstructed intensity and phase images of the living cancer cells; j) Schematic optical setup of the materfaces for TIE-based phase retrieval. (a, b) Reproduced with permission.[154] Copyright 2021, Springer Nature. (c-e) Reproduced with permission.[159] Copyright 2023, Optical Society of America. (f) Reproduced with permission.[156] Copyright 2022, Springer Nature. (g-i) Reproduced with permission.[160] Copyright 2024, American Association for the Advancement of Science. (j) Reproduced with permission.[161] Copyright 2021, American Chemical Society.

phase simultaneously with a moveable aperture.[153] Additionally, significant advancements have been made in phase imaging when integrated with computational imaging algorithms. However, existing methods are limited by complex structures or time-consuming algorithms, which constrains the performance of phase imaging for compact and real-time multidimensional imaging systems.

The exceptional modulation capabilities of metasurfaces can reduce the complexity of reconstruction algorithms and enhance reconstruction accuracy, paving the way for the development of high-resolution, high-dynamic-range phase imaging technologies. One method is to design an angle-sensitive metasurface, enabling the retrieval of the phase gradient of incident light and subsequently reconstructing the phase. As shown in **Figure 5a**, Yi et al. proposed an angle-based wavefront sensor enabled by the near-field effect of the metallic metasurface.[154] The metasurface with hole-shape unit cells is integrated into an image sensor, where 4 sensor pixels are covered by a unit cell. Utilizing the near-filed effects that are sensitive to the angle of the incident, a database is constructed according to the intensity ratio of the 4-pixel cell. Through the proposed wavefront sensor, the temporal dynamics of a surface during a fast-coagulating process can be observed in real-time. It is worth noting that the allowed angle range of the incident reaches 30°, which is 500 times larger than traditional Shack-Hartmann sensors. Additionally, Liu et al. report a phase image sensor based on asymmetric metasurfaces, the reflection of which is sensitively dependent on the incident angle. The phase gradient distribution can be obtained through such a metasurfaces array.[155] Figure 5f shows a schematic of a quantitative phase contrast imaging through a non-local metasurface by Ji et al. Due to the presence of non-localized guided-mode resonances, a high-Q resonance can be excited by paraxial rays and exhibit angular sensitivity.[156] The resonance also ensures a phase shift of $\pi/2$ with respect to the non-paraxial incident. Thus, the metasurface can be regarded as an angular filter to perform phase contrast imaging. The results of the contrast imaging demonstrate that the proposed phase contrast approach achieves an accuracy of 0.02 π.

Furthermore, interferometry can also be employed for phase imaging, as the interference terms of the electric field can modulate the phase information and subsequently convert it into intensity information for recording. In 2019, Bouchal et al. utilized the resonance and interference effects of plasmonic metasurface

metallic nanoantennas, combined with a microscopic system, to achieve the observation of the phase of meta-atoms in the phase-gradient metasurface.[157] In 2020, Kwon reported a single-shot quantitative phase gradient microscopy (QGPM) system based on a bi-layer shear interference metalens.[158] Each metalens has 2 focuses, and they are combined to perform as 4-f systems, where the incident light can undergo shear interference at a small distance of 2.25 μm compared with traditional shearing interferometers. As a result, the QGPM they proposed can clearly capture phase gradient information as small as 92.3 mrad μm^{-1} and achieve a spatial resolution of 2.76/3.48 μm in the x/y directions respectively. Wu et al. insert a pair of all-dielectric metasurfaces into a traditional microscope to achieve quantitative amplitude and phase imaging.[159] As shown in Figure 5c, the first metasurface splits a linearly polarized incident beam into 2 circularly polarized components, while the subsequent metasurface deflects both beams toward their initial propagation directions. The shear interference images in 4 linear polarizations are captured by the polarization camera, from which the phase gradient and intensity image can be reconstructed using the four-step phase shift method. In this way, Li et al. combined the design of metalens with shearing interference for a single-shot deterministic complex amplitude imaging.[160] With a phase gradient resolution of 42 mrad μm^{-1} and spatial resolution of 4.38 μm, the phase information in x and y directions, and the intensity image can be obtained simultaneously in a single shot with a monocular metasurface. The metasurfaces can independently achieve shear interference in the x and y directions on the image plane. As shown in Figure 5g, the linear polarized light was split into 2 RCP and 2 LCP beams and focused with a shear distance of Δs and an image distance "d". A polarization camera is placed on the image plane to capture the interference image of 4 linear polarization. In data post-processing, a four-step phase shift method was employed on the interference image to reconstruct the phase map and the intensity image. Meanwhile, Figure 5h,i also shows the phase and intensity of a living cancer cell by the metasurface proposed.

In addition to shearing interference and angle-based detection, transport-of-intensity equation (TIE) based phase retrieval is also a widely used method to acquire the phase information from an intensity map. Without the requirement of the complex optical setup, TIE-based phase retrieval can reconstruct the phase of the target from a series of defocused and in-focused images by solving the optical field transfer equation. In Figure 5j, Engay developed the TIE-based phase retrieval with metasurfaces, where the 2 images for solving can be obtained in a single-shot by utilizing the dielectric metasurface.[161] The metasurface is positioned in the Fourier plane of the 4-f system to generate 2 intensity-modulated images at distinct locations on the image plane. Subsequently, phase information is extracted from the acquired pair of images.

In conclusion, the development of metasurface-based phase imaging has made significant progress, offering various methods with unique advantages. However, there is still room for improvement and further exploration. Future research may focus on enhancing the resolution, sensitivity, and application scope of these techniques to meet the diverse needs of scientific and industrial fields.

7. Edge Imaging

The edge signal of an image, mathematically corresponding to the differential operation of the image, can also be regarded as one of the dimensions of the light field. Different from the dimensions related to the characteristics of electromagnetic waves mentioned above (polarization, intensity, frequency, phase), this is a dimension related to the overall incident light field and contains the intensity variation information of the image. The human visual system has a greater sensitivity to edge details compared with flat areas, making edge imaging a crucial aspect of human perception and interpretation of images.[162,163] Nowadays, image processing is typically done using integrated circuits, suffering from slow processing speeds and high-power consumption. Optical spatial differentiation methods can perform real-time, high-throughput image edge extraction and detection in a parallel manner, representing a significant innovation in existing image processing methods and devices.[164–167] In 2014, Silva et al. introduced the concept of computational metamaterials and simulated a 3-layer metasurface to achieve various optical computations including edge signal extraction.[168] With the development and maturity of nanotechnology and nano-fabrication technology, combining edge imaging with metasurfaces can provide new ideas for the design of new systems for edge detection in massive images, thereby overcoming the inherent speed limitations and power consumption issues of traditional methods.

Pan used a dielectric metasurface to implement the 2D Laplacian operation under *p*-polarized incidence.[164–167] At the Γ point, there is a symmetry-protected BICs that cannot be excited by external normal incident plane waves. In comparison, the quasi-BICs can partially couple with the incident plane wave. The quasi-BICs are gradually excited, and the transmittance increases with the increase of the incident angle, thus obtaining the transfer function required for differential operation. Zhou utilized similar principles to design dielectric metasurfaces for implementing Laplace operations, which can be integrated into optical microscopes and camera sensors to achieve edge imaging with a high NA.[169] By exploiting the interaction between the polarization of the input image and the polarization response of the metasurface, Cotrufo et al can unlock novel capabilities in the field of analog image processing for controllable orientation-dependent edge imaging: only the edges parallel to a certain direction, determined by the input polarization, are enhanced,[170] as shown in **Figure 6**a. Then, researchers utilized a similar structure to achieve high-resolution edge imaging with broadband dual-polarization.[171] Liu et al proposed a new method for implementing an optical spatial differentiator, which consists of a PB phase metasurface inserted between 2 orthogonally arranged linear polarizers, and can be used to achieve adjustable resolution broadband optical edge detection.[172] The design is realized by photonics spin-orbit interaction, which makes left- and right-handed photons with different spin angular momentum obtain opposite external orbital angular momentum, manifesting LCP and RCP images with a slight displacement at the image plane. The polarizer eliminates the overlapping components of the combined LCP and RCP, leaving only the edge information detectable. Bright-field imaging and phase-contrast imaging are 2 of the most representative operating modes in optical imaging

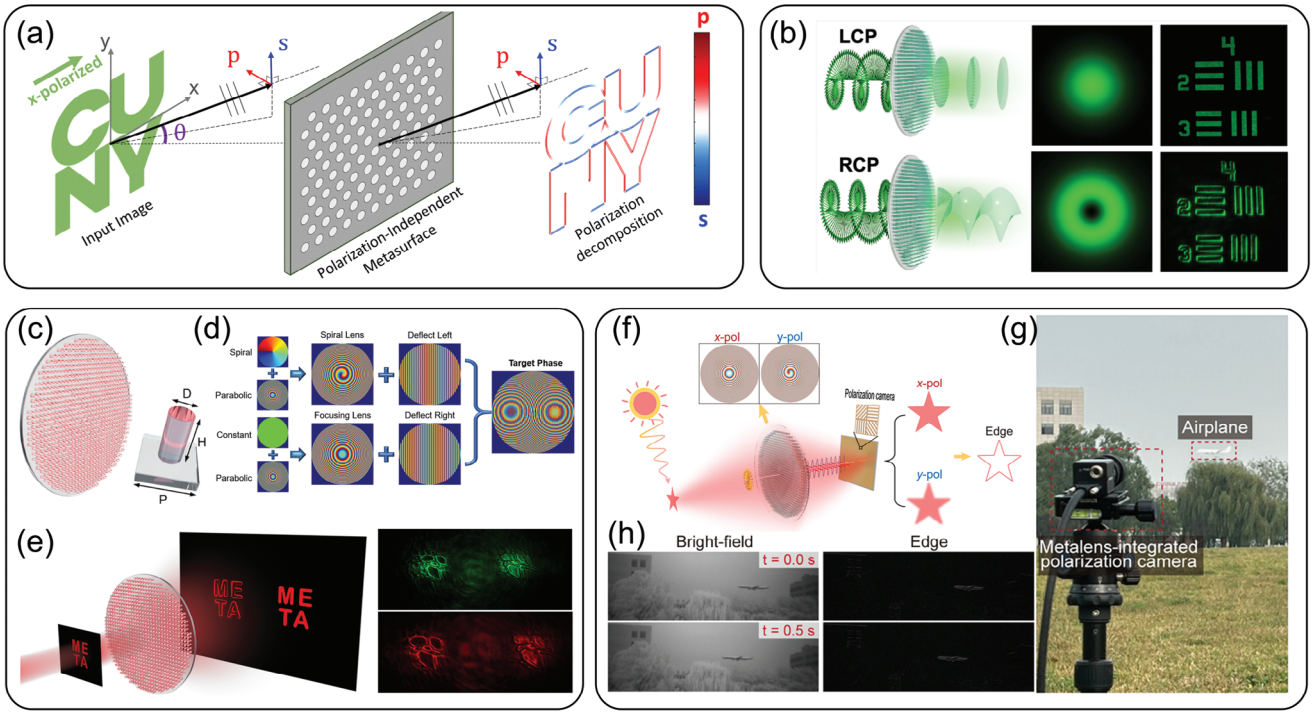

Figure 6. Edge imaging with metasurfaces. a) Schematic of the operational mechanism of an edge-detection metasurface highlighting the correlation between the orientation of edges and the polarization of the transmitted image through the metasurface; b) Spin-multiplexed metasurface capable of switching between bright-field and spiral phase contrast imaging modes; c) Schematic diagram of dielectric metasurface for edge imaging; d) Different phase design principles and distribution of metasurface; e) Schematic diagram of imaging principle based on the dielectric metasurface. The light field is modulated by the metasurface after the object, both the bright-field image containing all the information of the object and the spiral phase-contrast image with edge information appear simultaneously at the image plane; f) Schematic of polarization multiplexing metasurface for edge detection under incoherent illumination; g) An imaging system based on integrated metalens captures images of airplanes landing under natural outdoor light; h) Bright-field and edge-enhanced images of the flying airplane extracted from selected frames of the test. (a) Reproduced with permission.[170] Copyright 2023, Optical Society of America. (b) Reproduced with permission.[173] Copyright 2020, American Chemical Society. (c-e) Reproduced with permission.[175] Copyright 2023, American Chemical Society. (f-h) Reproduced with permission.[177] Copyright 2023, American Chemical Society.

systems. The former is suitable for conventional imaging of objects with clear contrast, while the latter is suitable for high-resolution imaging and analysis of fine structures and microscopic features. In 2020, researchers proposed a spin-multiplexed vortex-phase metasurface for implementing 2D spatial differentiation operations. Through a special design of different response characteristics to photon spins, this metasurface realized switchable and wide-wavelength edge-enhanced imaging,[173] as shown in Figure 6b. Zhang proposed a reconfigurable metasurface that can dynamically realize a series of functions by stretching the metasurface, including bright-field imaging, low-pass and high-pass filtering, and edge imaging.[174] Subsequently, Xu et al. designed a dielectric metasurface, as shown in Figure 6c. The spiral phase and constant phase are combined with the parabolic focusing phase to achieve the spiral lens phase and focusing lens phase, respectively.[175] By controlling the deflection phase, light waves with different phase structures can be separated into different spatial positions, thus achieving edge imaging and bright field imaging synchronously in the same field of view, as shown in Figure 6e. One key issue raised by optical edge imaging systems is the need for coherent laser light sources for illumination. Whereas in practical applications, most imaging systems use natural incoherent light as the illumination source. Tanriover proposed a subwavelength metallic metasurface that achieves 2D isotropic, polarization-independent broadband edge detection in the visible light frequency range under coherent and incoherent illumination.[176] In 2024, Yang et al proposed an imaging system based on polarized multiplexing metalens, which can achieve edge imaging under natural incoherent light illumination conditions,[177] as shown in Figure 6f. By designing a polarized multiplexing metalens to obtain the polarization-related optical transfer function, subtracting the 2 transfer functions results in an equivalent transfer function with a high-pass filtering response, which can achieve isotropic edge imaging. The researcher conducted experiments outdoors based on an imaging system integrated with metalens, capturing images of airplanes landing under natural lighting, as shown in Figure 6g. The bright-field images of the test and its corresponding edge-enhanced image are shown in Figure 6h. Compared with the method of edge imaging implemented by numerical convolution, this method greatly reduces the computational complexity and improves the calculation speed.

In summary, edge imaging utilizing metasurfaces significantly enhances the acquisition and interpretation of spatial information, thereby contributing to the broader context of multidimensional imaging. By leveraging the unique properties of metasurfaces, researchers have developed innovative methods that

enable real-time, high-throughput edge detection while addressing the limitations of traditional image processing techniques.

8. Conclusion

In this review, we summarized the recent advancements in metasurface research for multi-dimensional imaging. We commence by elucidating the fundamental principles of metasurface control over light and subsequently introduce various techniques such as the generalized Snell's law, geometric phase, resonant phase, propagation phase, and other methodologies that are crucial for manipulating the wavefront of light. The mathematical processes and solution methods of computational imaging, which play an important role in metasurface imaging, are also introduced. We introduce and summarize the principles of metasurface imaging in space imaging, polarization imaging, spectral imaging, phase imaging, and edge imaging. Moreover, we present an overview of the latest advancements in space imaging. For 2D imaging, we introduced developments such as single-wavelength metalenses, and achromatic metalenses. For 3D spatial imaging, we introduce developments such as achromatic light field cameras employing metalens arrays, and depth sensing techniques facilitated by metalenses. For metasurfaces used in polarization imaging, we systematically classify the current state of research and present various implementation approaches, encompassing polarization separation, polarization filtering, and algorithm-based methodologies. Following that, we introduce metasurfaces used for spectral imaging, including dispersion metasurfaces, narrowband filtering metasurfaces, and methods based on algorithmic reconstruction, with the help of advanced computational imaging algorithms, it has made significant progress in both spectral resolution and spatial resolution. We introduce metasurfaces for phase imaging based on principles, which include angle-sensitive near-field effects, interference modulation, and phase recovery algorithms. The research progress of the metasurface-based edge imaging was also introduced.

Despite significant theoretical and experimental advancements in multidimensional imaging with metasurfaces, there remains room for improvement in the dimensions and density of information that can be obtained. Researchers continue to explore the limits of the multidimensional imaging capabilities of metasurfaces. Achieving high-performance multidimensional imaging holds great promise for the miniaturization and integration of imaging devices, which is of paramount importance in the field.

Acknowledgements

National Natural Science Foundation of China (U22A20258, 12122406, 12192253, and 12274239), National Key Research and Development Program of China (2021YFA1400601 and 2022YFA1404501), the National Natural Science Fund for Distinguished Young Scholar (11925403), and the Natural Science Foundation of Tianjin (22JCYBJC00800, 22JCYBJC01350, and 22JCZDJC00400).

Conflict of Interest

The authors declare no conflict of interest.

Keywords

metasurfaces, multidimensional, optical imaging, phase, polarization

Received: July 8, 2024
Revised: October 15, 2024
Published online:

[1] W. Kühlbrandt, *Science* **2014**, *343*, 1443.
[2] Y. Yang, J. Seong, M. Choi, J. Park, G. Kim, H. Kim, J. Jeong, C. Jung, J. Kim, G. Jeon, K. Lee, D. H. Yoon, J. Rho, *Light Sci. Appl.* **2023**, *12*, 152.
[3] M. Broxton, L. Grosenick, S. Yang, N. Cohen, A. Andalman, K. Deisseroth, M. Levoy, *Opt. Express* **2013**, *21*, 25418.
[4] T. E. Bishop, P. Favaro, *IEEE Transact. Pattern Analysis Mach. Intel.* **2012**, *34*, 972.
[5] L. Yi, B. Hou, H. Zhao, X. Liu, *Nature* **2023**, *618*, 281.
[6] P. R. Griffiths, J. A. de Haseth, *Four. Transform Infr. Spectrom*. **2007**.
[7] Z. Yang, T. Albrow-Owen, W. Cai, T. Hasan, *Science* **2021**, *371*, eabe0722.
[8] S. G. Demos, R. R. Alfano, *Appl. Opt.* **1997**, *36*, 150.
[9] V. Gruev, R. Perkins, T. York, *Opt. Express* **2010**, *18*, 19087.
[10] B. Das, N. S. Bisht, R. V. Vinu, R. K. Singh, *Appl. Opt.* **2017**, *56*, 4591.
[11] L. Waller, M. Tsang, S. Ponda, S. Y. Yang, G. Barbastathis, *Opt. Express* **2011**, *19*, 2805.
[12] H. Park, K. B. Crozier, *Sci. Rep*. **2013**, *3*, 2460.
[13] G. A. Shaw, H. K. Burke, *Lincoln Lab. J.* **2003**, *14*, 3.
[14] T. Zimmermann, J. Rietdorf, R. Pepperkok, *FEBS Lett.* **2003**, *546*, 87.
[15] O. Fleischmann, R. Koch, in *Pattern Recognition* (Eds.: X. Jiang, J. Hornegger, R. Koch), Springer International Publishing, Cham, **2014**, 410–420.
[16] Q. Guo, Z. Shi, Y.-W. Huang, E. Alexander, C.-W. Qiu, F. Capasso, T. Zickler, *Proc. Natl. Acad. Sci. U.S.A.* **2019**, *116*, 22959.
[17] N. Yu, P. Genevet, M. A. Kats, F. Aieta, J.-P. Tetienne, F. Capasso, Z. Gaburro, *Science* **2011**, *334*, 333.
[18] R. Zhao, L. Huang, Y. Wang, *PhotoniX* **2020**, *1*, 20.
[19] J. Hu, X. Zhao, Y. Lin, A. Zhu, X. Zhu, P. Guo, B. Cao, C. Wang, *Sci. Rep.* **2017**, *7*, 41893.
[20] Z. Li, W. Liu, D. Ma, S. Yu, H. Cheng, D.-Y. Choi, J. Tian, S. Chen, *Phys. Rev. Appl.* **2022**, *17*, 024008.
[21] W. Liu, Z. Li, M. A. Ansari, H. Cheng, J. Tian, X. Chen, S. Chen, *Adv. Mater.* **2023**, *35*, 2208884.
[22] S. Park, G. Lee, B. Park, Y. Seo, C. bin Park, Y. T. Chun, C. Joo, J. Rho, J. M. Kim, J. Hone, S. C. Jun, *Light Sci. Appl.* **2020**, *9*, 98.
[23] G. Lee, J. Park, W. Choi, B. Ji, M. Kim, J. Rho, *Appl. Phys. Lett.* **2024**, *123*, 081705.
[24] P. D. Terekhov, V. E. Babicheva, K. V. Baryshnikova, A. S. Shalin, A. Karabchevsky, A. B. Evlyukhin, *Phys. Rev. B* **2019**, *99*, 045424.
[25] W. Liu, Z. Li, H. Cheng, S. Chen, J. Tian, *Phys. Rev. Appl.* **2017**, *8*, 014012.
[26] G. Qu, W. Yang, Q. Song, Y. Liu, C. W. Qiu, J. Han, D. P. Tsai, S. Xiao, *Nat. Commun.* **2020**, *11*, 5484.
[27] G. Zheng, H. Muhlenbernd, M. Kenney, G. Li, T. Zentgraf, S. Zhang, *Nat. Nanotechnol.* **2015**, *10*, 308.
[28] J. Li, W. Liu, H. Xu, Z. Huang, J. Wang, J. Wen, J. Yang, J. Guan, S. Wang, A. Alù, Z. Zhou, S. Chen, L. Chen, *Laser Photonics Rev.* **2024**, 2300729.
[29] I. Koirala, S.-S. Lee, D.-Y. Choi, *Opt. Express* **2018**, *26*, 18320.
[30] Z. Li, G. Geng, J. Cheng, W. Liu, S. Yu, B. Xie, H. Cheng, J. Li, W. Zhou, J. Tian, S. Chen, *Adv. Opt. Mater.* **2022**, *10*, 2200185.

[31] J. Li, G. Hu, L. Shi, N. He, D. Li, Q. Shang, Q. Zhang, H. Fu, L. Zhou, W. Xiong, J. Guan, J. Wang, S. He, L. Chen, *Nat. Commun.* **2021**, *12*, 6425.
[32] M. L. Tseng, M. Semmlinger, M. Zhang, C. Arndt, T.-T. Huang, J. Yang, H. Y. Kuo, V.-C. Su, M. K. Chen, C. H. Chu, B. Cerjan, D. P. Tsai, P. Nordlander, N. J. Halas, *Sci. Adv.* **2022**, *8*, eabn5644.
[33] G. Li, S. Zhang, T. Zentgraf, *Nat. Rev. Mater.* **2017**, *2*, 17010.
[34] Y. Yuan, K. Zhang, B. Ratni, Q. Song, X. Ding, Q. Wu, S. N. Burokur, P. Genevet, *Nat. Commun.* **2020**, *11*, 4186.
[35] A. Pors, M. G. Nielsen, S. I. Bozhevolnyi, *Optica, OPTICA* **2015**, *2*, 716.
[36] E. Maguid, I. Yulevich, D. Veksler, V. Kleiner, M. L. Brongersma, E. Hasman, *Science* **2016**, *352*, 1202.
[37] D. Ma, Z. Li, W. Liu, G. Geng, H. Cheng, J. Li, J. Tian, S. Chen, *Adv. Opt. Mater.* **2022**, *10*, 2102628.
[38] C. C. Nadell, B. Huang, J. M. Malof, W. J. Padilla, *Opt. Express* **2019**, *27*, 27523.
[39] H. Ren, X. Fang, J. Jang, J. Bürger, J. Rho, S. A. Maier, *Nat. Nanotechnol.* **2020**, *15*, 948.
[40] B. Xiong, Y. Liu, Y. Xu, L. Deng, C.-W. Chen, J.-N. Wang, R. Peng, Y. Lai, Y. Liu, M. Wang, *Science* **2023**, *379*, 294.
[41] B. Yang, W. Liu, Z. Li, H. Cheng, D.-Y. Choi, S. Chen, J. Tian, *Nano Lett.* **2019**, *19*, 4221.
[42] A. Barulin, Y. Kim, D. K. Oh, J. Jang, H. Park, J. Rho, I. Kim, *Nat. Commun.* **2024**, *15*, 26.
[43] T. Badloe, I. Kim, Y. Kim, J. Kim, J. Rho, *Adv. Sci.* **2021**, *8*, 2102646.
[44] I. Staude, A. E. Miroshnichenko, M. Decker, N. T. Fofang, S. Liu, E. Gonzales, J. Dominguez, T. S. Luk, D. N. Neshev, I. Brener, Y. Kivshar, *ACS Nano* **2013**, *7*, 7824.
[45] A. I. Kuznetsov, A. E. Miroshnichenko, M. L. Brongersma, Y. S. Kivshar, B. Luk'yanchuk, *Science* **2016**, *354*, aag2472.
[46] M. K. Hedayati, M. Elbahri, *Plasmonics* **2017**, *12*, 1463.
[47] M. Song, L. Feng, P. Huo, M. Liu, C. Huang, F. Yan, Y. Lu, T. Xu, *Nat. Nanotechnol.* **2022**, *18*, 71.
[48] S. Chen, Z. Li, W. Liu, H. Cheng, J. Tian, *Adv. Mater.* **2019**, *31*, 1802458.
[49] M. S. Bin-Alam, O. Reshef, Y. Mamchur, M. Z. Alam, G. Carlow, J. Upham, B. T. Sullivan, J.-M. Ménard, M. J. Huttunen, R. W. Boyd, K. Dolgaleva, *Nat. Commun.* **2021**, *12*, 974.
[50] N. Meinzer, W. L. Barnes, I. R. Hooper, *Nature Photon.* **2014**, *8*, 889.
[51] C. Pelzman, S.-Y. Cho, *Appl. Phys. Lett.* **2015**, *106*, 251101.
[52] C. Sauvan, J. P. Hugonin, I. S. Maksymov, P. Lalanne, *Phys. Rev. Lett.* **2013**, *110*, 237401.
[53] D. Sell, J. Yang, E. W. Wang, T. Phan, S. Doshay, J. A. Fan, *ACS Photonics* **2018**, *5*, 2402.
[54] A. B. Evlyukhin, B. N. Chichkov, *Phys. Rev. B* **2019**, *100*, 125415.
[55] H. Li, Y. Xu, X. Zhang, X. Xiao, F. Zhou, Z. Zhang, *Opt. Express* **2022**, *30*, 28954.
[56] A. A. Basharin, M. Kafesaki, E. N. Economou, C. M. Soukoulis, V. A. Fedotov, V. Savinov, N. I. Zheludev, *Phys. Rev. X* **2015**, *5*, 011036.
[57] W. Ma, Y. Xu, B. Xiong, L. Deng, R. Peng, M. Wang, Y. Liu, *Adv. Mater.* **2022**, 2110022.
[58] S. Wang, P. C. Wu, V.-C. Su, Y.-C. Lai, C. Hung Chu, J.-W. Chen, S.-H. Lu, J. Chen, B. Xu, C.-H. Kuan, T. Li, S. Zhu, D. P. Tsai, *Nat. Commun.* **2017**, *8*, 187.
[59] N. Yu, F. Capasso, *Nat. Mater.* **2014**, *13*, 139.
[60] A. Pors, S. I. Bozhevolnyi, *Opt. Express* **2013**, *21*, 27438.
[61] J. C. Gutiérrez-Vega, *Opt. Lett.* **2011**, *36*, 1143.
[62] L. Huang, X. Chen, H. Mühlenbernd, G. Li, B. Bai, Q. Tan, G. Jin, T. Zentgraf, S. Zhang, *Nano Lett.* **2012**, *12*, 5750.
[63] M. Pan, Y. Fu, M. Zheng, H. Chen, Y. Zang, H. Duan, Q. Li, M. Qiu, Y. Hu, *Light Sci. Appl.* **2022**, *11*, 195.
[64] M. Khorasaninejad, A. Y. Zhu, C. Roques-Carmes, W. T. Chen, J. Oh, I. Mishra, R. C. Devlin, F. Capasso, *Nano Lett.* **2016**, *16*, 7229.
[65] W. Liu, Z. Li, H. Cheng, S. Chen, *iScience* **2020**, *23*, 101868.
[66] S. W. Marcus, A. Epstein, *Phys. Rev. B* **2019**, *100*, 115144.
[67] P. Genevet, F. Capasso, *Rep. Prog. Phys.* **2015**, *78*, 024401.
[68] I. Kim, H. Jeong, J. Kim, Y. Yang, D. Lee, T. Badloe, G. Kim, J. Rho, *Adv. Opt. Mater.* **2021**, *9*, 2100609.
[69] M. V. Berry, *Proc. Royal Soc. London. A. Mathemat. Phys. Sci.* **1997**, *392*, 45.
[70] S. Pancharatnam, S. Pancharatnam, *Resonance* **2013**, *18*, 387.
[71] Y. Peng, J. Zhang, X. Zhou, C. Chen, T. Guo, Q. Yan, Y. Zhang, C. Wu, *Laser Photonics Rev.* **2024**, 2300731.
[72] Z. Yu, H. Li, W. Zhao, P.-S. Huang, Y.-T. Lin, J. Yao, W. Li, Q. Zhao, P. C. Wu, B. Li, P. Genevet, Q. Song, P. Lai, *Nat. Commun.* **2024**, *15*, 2607.
[73] J. Kim, D. Jeon, J. Seong, T. Badloe, N. Jeon, G. Kim, J. Kim, S. Baek, J.-L. Lee, J. Rho, *ACS Nano* **2022**, *16*, 3546.
[74] M. Khorasaninejad, W. T. Chen, J. Oh, F. Capasso, *Nano Lett.* **2016**, *16*, 3732.
[75] Y. Hu, X. Wang, X. Luo, X. Ou, L. Li, Y. Chen, P. Yang, S. Wang, H. Duan, *Nanophotonics* **2020**, *9*, 3755.
[76] S. Gao, C.-S. Park, S.-S. Lee, D.-Y. Choi, *Adv. Opt. Mater.* **2019**, *7*, 1801337.
[77] Y. Intaravanne, X. Chen, *Nanophotonics* **2020**, *9*, 1003.
[78] J. P. Balthasar Mueller, N. A. Rubin, R. C. Devlin, B. Groever, F. Capasso, *Phys. Rev. Lett.* **2017**, *118*, 113901.
[79] Y. Fan, J. Chu, R. Zhang, C. Guan, J. Liu, *Photon. Res.* **2023**, *11*, 1975.
[80] K. Yao, Y. Zheng, *J. Phys. Chem. C* **2019**, *123*, 11814.
[81] Z. Shen, S. Fan, W. Yin, S. Li, Y. Xu, L. Zhang, X. Chen, *Laser Photonics Rev.* **2022**, *16*, 2200370.
[82] Z. Li, D. Rosenmann, D. A. Czaplewski, X. Yang, J. Gao, *Opt. Express* **2019**, *27*, 28313.
[83] J. Hong, J. van de Groep, N. Lee, S. J. Kim, P. Lalanne, P. G. Kik, M. L. Brongersma, *Optica* **2023**, *10*, 134.
[84] J. W. den Herder, A. C. Brinkman, S. M. Kahn, G. Branduardi-Raymont, K. Thomsen, H. Aarts, M. Audard, J. V. Bixler, A. J. den Boggende, J. Cottam, T. Decker, L. Dubbeldam, C. Erd, H. Goulooze, M. Güdel, P. Guttridge, C. J. Hailey, K. A. Janabi, J. S. Kaastra, P. A. J. de Korte, B. J. van Leeuwen, C. Mauche, A. J. McCalden, R. Mewe, A. Naber, F. B. Paerels, J. R. Peterson, A. P. Rasmussen, K. Rees, I. Sakelliou, et al., *A&A* **2001**, *365*, L7.
[85] Q. Li, X. He, Y. Wang, H. Liu, D. Xu, F. Guo, *J. Biomed. Opt.* **2013**, *18*, 100901.
[86] T. Xu, Y.-K. Wu, X. Luo, L. J. Guo, *Nat. Commun.* **2010**, *1*, 59.
[87] R. Chai, Q. Liu, W. Liu, Z. Li, H. Cheng, J. Tian, S. Chen, *ACS Photonics* **2023**, *10*, 2031.
[88] C. W. Hsu, B. Zhen, A. D. Stone, J. D. Joannopoulos, M. Soljačić, *Nat. Rev. Mater.* **2016**, *1*, 16048.
[89] C. Chen, S. Gao, W. Song, H. Li, S.-N. Zhu, T. Li, *Nano Lett.* **2021**, *21*, 1815.
[90] B. Redding, S. F. Liew, R. Sarma, H. Cao, *Nature Photon.* **2013**, *7*, 746.
[91] B. Redding, S. F. Liew, Y. Bromberg, R. Sarma, H. Cao, *Optica* **2016**, *3*, 956.
[92] P. Wang, R. Menon, *Opt. Express* **2014**, *22*, 14575.
[93] A. Bhandari, A. Kadambi, R. Raskar, Computational Imaging, MIT Press, **2022**.
[94] G. Barbastathis, A. Ozcan, G. Situ, *Optica, OPTICA* **2019**, *6*, 921.
[95] M. Bertero, P. Boccacci, C. De Mol, *Introduction to Inverse Problems in Imaging*, CRC Press, Boca Raton, **2021**.
[96] J. A. Fessler, *IEEE Transact. Med. Imag.* **1994**, *13*, 290.
[97] M. E. Gehm, R. John, D. J. Brady, R. M. Willett, T. J. Schulz, *Opt. Express* **2007**, *15*, 14013.
[98] C. G. Graff, E. Y. Sidky, *Appl. Opt.* **2015**, *54*, C23.
[99] D. L. Donoho, *IEEE Trans. Inf. Theory* **2006**, *52*, 1289.

[100] N. Nguyen, P. Milanfar, G. Golub, *IEEE Transact. Image Process.* **2001**, *10*, 573.
[101] A. Sinha, J. Lee, S. Li, G. Barbastathis, *Optica* **2017**, *4*, 1117.
[102] X. Dun, H. Ikoma, G. Wetzstein, Z. Wang, X. Cheng, Y. Peng, *Optica* **2020**, *7*, 913.
[103] L. Huang, R. Luo, X. Liu, X. Hao, *Light Sci. Appl.* **2022**, *11*, 61.
[104] W. Shi, F. Jiang, S. Liu, D. Zhao, *IEEE Transact. Image Process.* **2020**, *29*, 375.
[105] J. Hunt, T. Driscoll, A. Mrozack, G. Lipworth, M. Reynolds, D. Brady, D. R. Smith, *Science* **2013**, *339*, 310.
[106] Y. Luo, Y. Zhao, J. Li, E. Çetintaş, Y. Rivenson, M. Jarrahi, A. Ozcan, *eLight* **2022**, *2*, 4.
[107] J. B. Pendry, *Phys. Rev. Lett.* **2000**, *85*, 3966.
[108] S. Park, C. Park, Y. J. Hwang, J. Kang, G. Lee, Y. Seo, Y. T. Chun, J. Rho, J. M. Kim, J. Hone, S. C. Jun, *Adv. Opt. Mater.* **2021**, *9*, 2001526.
[109] J. Park, G. Lee, D. Lee, M. Kim, J. Rho, *Nanomaterials* **2022**, *12*, 1019.
[110] R. Zuo, W. Liu, H. Cheng, S. Chen, J. Tian, *Adv. Opt. Mater.* **2018**, *6*, 1800795.
[111] M. Khorasaninejad, W. T. Chen, R. C. Devlin, J. Oh, A. Y. Zhu, F. Capasso, *Science* **2016**, *352*, 1190.
[112] R. Paniagua-Domínguez, Y. F. Yu, E. Khaidarov, S. Choi, V. Leong, R. M. Bakker, X. Liang, Y. H. Fu, V. Valuckas, L. A. Krivitsky, A. I. Kuznetsov, *Nano Lett.* **2018**, *18*, 2124.
[113] J.-S. Park, S. W. D. Lim, A. Amirzhan, H. Kang, K. Karrfalt, D. Kim, J. Leger, A. Urbas, M. Ossiander, Z. Li, F. Capasso, *ACS Nano* **2024**, *18*, 3187.
[114] J. Kim, J. Seong, W. Kim, G.-Y. Lee, S. Kim, H. Kim, S.-W. Moon, D. K. Oh, Y. Yang, J. Park, J. Jang, Y. Kim, M. Jeong, C. Park, H. Choi, G. Jeon, K. Lee, D. H. Yoon, N. Park, B. Lee, H. Lee, J. Rho, *Nat. Mater.* **2023**, *22*, 474.
[115] Y. Deng, X. Wang, Z. Gong, K. Dong, S. Lou, N. Pégard, K. B. Tom, F. Yang, Z. You, L. Waller, J. Yao, *Adv. Mater.* **2018**, *30*, 1802632.
[116] J. Chen, X. Ye, S. Gao, Y. Chen, Y. Zhao, C. Huang, K. Qiu, S. Zhu, T. Li, *Optica* **2022**, *9*, 431.
[117] F. Aieta, M. A. Kats, P. Genevet, F. Capasso, *Science* **2015**, *347*, 1342.
[118] W. T. Chen, A. Y. Zhu, V. Sanjeev, M. Khorasaninejad, Z. Shi, E. Lee, F. Capasso, *Nat. Nanotech.* **2018**, *13*, 220.
[119] S. Baek, J. Kim, Y. Kim, W. Seok Cho, T. Badloe, S.-W. Moon, J. Rho, J.-L. Lee, *Photon. Res.* **2022**, *10*, B30.
[120] W. T. Chen, A. Y. Zhu, J. Sisler, Z. Bharwani, F. Capasso, *Nat. Commun.* **2019**, *10*, 355.
[121] Y. Wang, Q. Chen, W. Yang, Z. Ji, L. Jin, X. Ma, Q. Song, A. Boltasseva, J. Han, V. M. Shalaev, S. Xiao, *Nat. Commun.* **2021**, *12*, 5560.
[122] H. Ren, J. Jang, C. Li, A. Aigner, M. Plidschun, J. Kim, J. Rho, M. A. Schmidt, S. A. Maier, *Nat. Commun.* **2022**, *13*, 4183.
[123] Z. Li, R. Pestourie, J.-S. Park, Y.-W. Huang, S. G. Johnson, F. Capasso, *Nat. Commun.* **2022**, *13*, 2409.
[124] X. Xiao, Y. Zhao, X. Ye, C. Chen, X. Lu, Y. Rong, J. Deng, G. Li, S. Zhu, T. Li, *Light Sci. Appl.* **2022**, *11*, 323.
[125] Q. Chen, Y. Gao, S. Pian, Y. Ma, *Phys. Rev. Lett.* **2023**, *131*, 193801.
[126] R. J. Lin, V.-C. Su, S. Wang, M. K. Chen, T. L. Chung, Y. H. Chen, H. Y. Kuo, J.-W. Chen, J. Chen, Y.-T. Huang, J.-H. Wang, C. H. Chu, P. C. Wu, T. Li, Z. Wang, S. Zhu, D. P. Tsai, *Nat. Nanotechnol.* **2019**, *14*, 227.
[127] Q. Fan, W. Xu, X. Hu, W. Zhu, T. Yue, C. Zhang, F. Yan, L. Chen, H. J. Lezec, Y. Lu, A. Agrawal, T. Xu, *Nat. Commun.* **2022**, *13*, 2130.
[128] W. Liu, D. Ma, Z. Li, H. Cheng, D.-Y. Choi, J. Tian, S. Chen, *Optica* **2020**, *7*, 1706.
[129] S. Shibata, N. Hagen, Y. Otani, *Opt. Lett.* **2019**, *44*, 891.
[130] S. Gao, C. Zhou, W. Liu, W. Yue, S. Chen, S. Lee, D. Choi, Y. Li, *Laser Photonics Rev.* **2022**, *16*, 2100603.
[131] C. Zhang, J. Hu, Y. Dong, A. Zeng, H. Huang, C. Wang, *Photon. Res.* **2021**, *9*, 583.
[132] Y. Ren, S. Guo, W. Zhu, P. Huo, S. Liu, S. Zhang, P. Chen, L. Chen, H. J. Lezec, A. Agrawal, Y. Lu, T. Xu, *Adv. Photonics Res.* **2022**, *3*, 2100373.
[133] N. Yu, F. Aieta, P. Genevet, M. A. Kats, Z. Gaburro, F. Capasso, *Nano Lett.* **2012**, *12*, 6328.
[134] Z. Li, W. Liu, H. Cheng, D. Choi, S. Chen, J. Tian, *Adv. Mater.* **2020**, *32*, 1907983.
[135] N. A. Rubin, G. D'Aversa, P. Chevalier, Z. Shi, W. T. Chen, F. Capasso, *Science* **2019**, *365*, eaax1839.
[136] A. Basiri, X. Chen, J. Bai, P. Amrollahi, J. Carpenter, Z. Holman, C. Wang, Y. Yao, *Light Sci. Appl.* **2019**, *8*, 78.
[137] J. Zuo, J. Bai, S. Choi, A. Basiri, X. Chen, C. Wang, Y. Yao, *Light Sci. Appl.* **2023**, *12*, 218.
[138] Z. Huang, Y. Zheng, J. Li, Y. Cheng, J. Wang, Z.-K. Zhou, L. Chen, *Nano Lett.* **2023**, *23*, 10991.
[139] Q. Fan, W. Xu, X. Hu, W. Zhu, T. Yue, F. Yan, P. Lin, L. Chen, J. Song, H. J. Lezec, A. Agrawal, Y. Lu, T. Xu, *Nat. Commun.* **2023**, *14*, 7180.
[140] Y. Garini, I. T. Young, G. McNamara, *Cytometry Pt A* **2006**, *69A*, 735.
[141] S. Rao, Y. Huang, K. Cui, Y. Li, *Optica* **2022**, *9*, 1253.
[142] Z. Zhang, Y. Liu, Z. Wang, Y. Zhang, X. Guo, S. Xiao, K. Xu, Q. Song, *Nano Lett.* **2023**, *23*, 3459.
[143] X. Hua, Y. Wang, S. Wang, X. Zou, Y. Zhou, L. Li, F. Yan, X. Cao, S. Xiao, D. P. Tsai, J. Han, Z. Wang, S. Zhu, *Nat. Commun.* **2022**, *13*, 2732.
[144] Y. Li, X. Jiang, Y. Chen, Y. Wang, Y. Wu, D. Yu, K. Wang, S. Bai, S. Xiao, Q. Song, *Light Sci. Appl.* **2023**, *12*, 184.
[145] A. Tittl, A. Leitis, M. Liu, F. Yesilkoy, D.-Y. Choi, D. N. Neshev, Y. S. Kivshar, H. Altug, *Science* **2018**, *360*, 1105.
[146] F. Yesilkoy, E. R. Arvelo, Y. Jahani, M. Liu, A. Tittl, V. Cevher, Y. Kivshar, H. Altug, *Nat. Photonics* **2019**, *13*, 390.
[147] A. McClung, S. Samudrala, M. Torfeh, M. Mansouree, A. Arbabi, *Sci. Adv.* **2020**, *6*, eabc7646.
[148] Z. Wang, S. Yi, A. Chen, M. Zhou, T. S. Luk, A. James, J. Nogan, W. Ross, G. Joe, A. Shahsafi, K. X. Wang, M. A. Kats, Z. Yu, *Nat. Commun.* **2019**, *10*, 1020.
[149] J. Yang, K. Cui, X. Cai, J. Xiong, H. Zhu, S. Rao, S. Xu, Y. Huang, F. Liu, X. Feng, W. Zhang, *Laser Photonics Rev.* **2022**, *16*, 2100663.
[150] F. Zernike, *Science* **1955**, *121*, 345.
[151] J. W. Goodman, R. W. Lawrence, *Appl. Phys. Lett.* **1967**, *11*, 77.
[152] V. Srinivasan, H. C. Liu, M. Halioua, *Appl. Opt.* **1984**, *23*, 3105.
[153] H. M. L. Faulkner, J. M. Rodenburg, *Phys. Rev. Lett.* **2004**, *93*, 023903.
[154] S. Yi, J. Xiang, M. Zhou, Z. Wu, L. Yang, Z. Yu, *Nat. Commun.* **2021**, *12*, 6002.
[155] J. Liu, H. Wang, Y. Li, L. Tian, R. Paiella, *Nanophotonics* **2023**, *12*, 3519.
[156] A. Ji, J.-H. Song, Q. Li, F. Xu, C.-T. Tsai, R. C. Tiberio, B. Cui, P. Lalanne, P. G. Kik, D. A. B. Miller, M. L. Brongersma, *Nat. Commun.* **2022**, *13*, 7848.
[157] P. Bouchal, P. Dvořák, J. Babocký, Z. Bouchal, F. Ligmajer, M. Hrtoň, V. Křápek, A. Faßbender, S. Linden, R. Chmelík, T. Šikola, *Nano Lett.* **2019**, *19*, 1242.
[158] H. Kwon, E. Arbabi, S. M. Kamali, M. Faraji-Dana, A. Faraon, *Nat. Photonics* **2020**, *14*, 109.
[159] Q. Wu, J. Zhou, X. Chen, J. Zhao, M. Lei, G. Chen, Y.-H. Lo, Z. Liu, *Optica* **2023**, *10*, 619.
[160] L. Li, S. Wang, F. Zhao, Y. Zhang, S. Wen, H. Chai, Y. Gao, W. Wang, L. Cao, Y. Yang, *Sci. Adv.* **2024**, *10*, eadl0501.
[161] E. Engay, D. Huo, R. Malureanu, A.-I. Bunea, A. Lavrinenko, *Nano Lett.* **2021**, *21*, 3820.
[162] S. He, R. Wang, H. Luo, *Nanophotonics* **2022**, *11*, 1083.
[163] J. Zhou, S. Liu, H. Qian, Y. Li, H. Luo, S. Wen, Z. Zhou, G. Guo, B. Shi, Z. Liu, *Sci. Adv.* **2020**, *6*, eabc4385.
[164] C. Zhou, Y. Chen, Y. Li, J. Li, R. Zhao, C. Tao, C. Liu, Y. Bai, X. Li, Y. Wang, L. Huang, *Adv. Funct. Mater.* **2024**, 2313777.
[165] T. Zhu, J. Huang, Z. Ruan, *Adv. Photon.* **2020**, *2*, 1.

[166] D. Zhu, Y.-H. Zhang, S.-J. Liu, W. Chen, L. Zhu, S.-J. Ge, P. Chen, W. Duan, Y.-Q. Lu, *Nano Lett.* **2024**, *24*, 140.
[167] A. Cordaro, H. Kwon, D. Sounas, A. F. Koenderink, A. Alù, A. Polman, *Nano Lett.* **2019**, *19*, 8418.
[168] A. Silva, F. Monticone, G. Castaldi, V. Galdi, A. Alù, N. Engheta, *Science* **2014**, *343*, 160.
[169] Y. Zhou, H. Zheng, I. I. Kravchenko, J. Valentine, *Nat. Photonics* **2020**, *14*, 316.
[170] M. Cotrufo, S. Singh, A. Arora, A. Majewski, A. Alù, *Optica* **2023**, *10*, 1331.
[171] M. Cotrufo, A. Arora, S. Singh, A. Alù, *Nat. Commun.* **2023**, *14*, 7078.
[172] J. Zhou, H. Qian, C.-F. Chen, J. Zhao, G. Li, Q. Wu, H. Luo, S. Wen, Z. Liu, *Proc. Natl. Acad. Sci. U.S.A.* **2019**, *116*, 11137.
[173] P. Huo, C. Zhang, W. Zhu, M. Liu, S. Zhang, S. Zhang, L. Chen, H. J. Lezec, A. Agrawal, Y. Lu, T. Xu, *Nano Lett.* **2020**, *20*, 2791.
[174] X. Zhang, Y. Zhou, H. Zheng, A. E. Linares, F. C. Ugwu, D. Li, H.-B. Sun, B. Bai, J. G. Valentine, *Nano Lett.* **2021**, *21*, 8715.
[175] Y. Zhang, P. Lin, P. Huo, M. Liu, Y. Ren, S. Zhang, Q. Zhou, Y. Wang, Y. Lu, T. Xu, *Nano Lett.* **2023**, *23*, 2991.
[176] I. Tanriover, S. A. Dereshgi, K. Aydin, *Nat. Commun.* **2023**, *14*, 6484.
[177] S. Wang, L. Li, S. Wen, R. Liang, Y. Liu, F. Zhao, Y. Yang, *Nano Lett.* **2023**, *24*, 356.

Qi Liu is a Ph.D. student at the School of Physics, Nankai University, China. He received his B.S. degree in physics in 2022 from Nankai University. His current research focuses on the application of metasurfaces in imaging.

Yongliang Liu is a Ph.D. student at the School of Physics, Nankai University, China. He received his M.E degree in Instrumentation Engineering in 2019 from North University of China. His current research focuses on the application of terahertz metasurfaces in optical field manipulation.

Shuqi Chen is a professor at the Key Laboratory of Weak Light Nonlinear Photonics, Ministry of Education, School of Physics and TEDA Institute of Applied Physics, Nankai University, China. He received his joint training Ph.D. degree from the University of Arizona, USA, and Nankai University, China, in 2009. His current research interests include nonlinear optics, phononics and acoustics metasurfaces, and subwavelength electromagnetics.